Pure Appl. Geophys. 178 (2021), 1021–1045

https://doi.org/10.1007/s00024-021-02677-3

Pure and Applied Geophysics

A New Ground Motion Model (GMM) for Northeast India (NEI) and Its Adjacent Countries for Interface Earthquakes Considering Both Strong Motion Records and Simulated Data

Tauhidur Rahman[1] and Ricky L. Chhangte[1]

Abstract—A ground motion model (GMM) for interface subduction zone earthquakes of Northeast India (NEI) and its adjacent countries is developed for the first time. Countries adjacent to NEI are Bangladesh, Bhutan, China, Myanmar and Nepal. High-magnitude earthquakes occur frequently in these regions due to buildup of high-stress parameters in the subduction zone of the Indian tectonic plate. Strong motion data are too few and sparse to develop a robust GMM for this region. We used both finite-fault simulations and a stochastic point-source model in developing our GMM. In our GMM, we used 50,000 ground motion samples which were stochastically simulated for different moment magnitudes (M_w) of 5.0–9.0 and hypocentral distances of 30–300 km using a point-source seismological stochastic model and finite fault model. In this study, we calculated stress drop ($\Delta\sigma$), quality factor $Q(f)$ and all other region-specific seismic input parameters from the past strong motion records of interface subduction zone earthquakes of NEI and its adjacent countries. We used these seismic input parameters in ground motion simulation. Sensitivity analyses of the input parameters were also performed to check the bias of the present model. Our GMM was validated by comparing it with the existing NEI interface strong motion records. We compared our GMM with other GMMs developed for interface subduction zone earthquakes for different regions in the world. We also compared our GMM with point-source and finite-fault simulation models. Ground motion parameters estimated using the point-source model are comparatively higher than the finite-fault simulation model. Horizontal components of peak ground acceleration (PGA) and spectral acceleration (S_a) can be estimated for NEI using our GMM.

1. Introduction

Region-specific ground motion models (GMMs) are used to estimate the seismic hazard at a site or in a region. Many researchers have developed GMMs for different regions of the world either with abundant available strong motion data or with numerical simulations when earthquake records are sparse. In this study, a GMM for interface subduction zone earthquakes in Northeast India (NEI) and its adjacent countries was developed with numerical simulation due to the small number of recorded events (12) in the region.

NEI has historically faced seismic threats due to its tectonic setting. Twenty large-magnitude ($M_w >$ 7.0) earthquakes have occurred in NEI and its adjacent countries since 1400 A.D. (Rahman 2012). Goswami and Sharma (1982) estimated the average recurrence interval of large-magnitude earthquakes ($M_w \geq 8.0$) in NEI and its adjacent countries as 25–30 years. Their prediction was based on Gumbel's theory of extreme events. Parvez and Ram (1997) estimated that the cumulative probability of occurrence of $M_w \geq 7.0$ earthquakes for NEI ranged from 0.881 to 0.995 for a period of 40 years. They also concluded that NEI should expect great earthquakes at any moment in the future. Sil et al. (2015) characterized NEI and adjoining regions as having a very high rate of seismicity. They predicted that in the future, there is a high probability of earthquakes of $M_w > 6$ in NEI and its adjacent countries, but did not estimate the seismic hazard from these earthquakes.

As per the Indian Standard (IS) Code of Practice IS 1893: 2016, India is divided into four seismic zones, namely II–V. Zones II–IV have seismic zone factors 0.1, 0.16 and 0.24, respectively. Seismic zone V has the highest zonal factor of 0.36 which is used for estimating the design horizontal seismic coefficient. Therefore, seismic zone V is considered the most severe seismic zone in India where many devastating earthquakes have already occurred. However, the design spectral acceleration values in

---

[1] Civil Engineering Department, National Institute of Technology, Silchar 788010, Assam, India. E-mail: tauhid_srm@yahoo.com; rickylchhangte@gmail.com

IS 1893: 2016 are based only on the historical seismicity of the region and do not consider various other seismic factors like active faults and their characterization. Upgrading of IS 1893: 2016 is essential to account for more current seismic hazard information on NEI that includes better characterization of seismic sources including active faults and other related seismic input parameters in the region.

In general, two types of earthquakes occur in NEI, namely crustal and subduction earthquakes. Crustal earthquakes occur above 15 km, and rare crustal earthquakes occur at deeper levels in NEI (Mitra et al. 2005; Chen and Molnar 1983). Young et al. (1997) described two types of subduction zone earthquakes: interface and intraslab. Subduction zone interface earthquakes are shallow-angle thrust events and occur at the interface between the subducting and overriding plates. Youngs et al. (1997) stated that GMMs for crustal and subduction zone earthquakes are different, and for each type of earthquake, separate GMMs are required. Lin and Lee (2008) also stated that ground motion parameters for intraslab subduction earthquakes are 20–30% higher than the interface subduction earthquakes.

The occurrence of interface seismic events is restricted to depths of 10–55 km (Llenos and McGuire 2007). Lin and Lee (2008) reported that interface subduction zone earthquakes occur at shallower depths. They described an interface earthquake in Taiwan with a focal depth of 5.65 km. Youngs et al. (1997) suggested that focal depths of interface subduction earthquakes are less than 50 km. Tichelaar and Ruff (1993) also suggested that interface subduction earthquakes take place at focal depths less than 50 km. Atkinson and Boore (2003) reported that the focal depths for interface earthquakes are less than 50 km. Therefore, in this study, we used focal depth criteria of 10–50 km to classify the interface subduction zone earthquakes in NEI and its adjacent countries to develop our GMM.

Tichelaar and Ruff (1993) described that the focal mechanism of interface subduction zone earthquakes is consistent with underthrusting. This implies that slip vector orientation mostly represents the thrust type of earthquake. Tichelaar and Ruff (1993) also discussed that the dip angles of fault planes for interface earthquakes are normally less than 35°.

The focal mechanisms of interface subduction earthquakes in NEI are quite complex and are predominantly thrust-type events consistent with underthusting and the slip vector orientation being mostly of the thrust type (Kundu and Galahaut 2012). In NEI, interface earthquakes are identified based on thrust-type events, shallow dip angles and focal depth. We fixed the focal depth limit for the interface subduction zone earthquakes of NEI and adjacent countries as 10–50 km. Dip angles for interface earthquakes in NEI and adjacent countries vary from 14° to 34°. The dip angles and focal depths for all the interface earthquake events used in this study are presented in Table 1.

Nath et al. (2012) proposed a GMM for the Shillong region located in NEI by considering 30 strong motion records. Earthquakes occurring in the Shillong region are crustal earthquakes. Gupta (2010) developed response spectral attenuation relations for in-slab earthquakes in the Indo-Burmese subduction zone considering only three strong motion records for M_w 7.2, 6.4 and 6.3. These GMMs are not valid for interface subduction zone earthquakes. Das et al. (2006) conducted seismic hazards analysis for NEI based on their GMM developed by combining earthquakes records both for crustal and subduction zone earthquakes. This model can also not be used categorically for the interface subduction zone earthquakes for NEI and adjacent countries.

To date, suitable region-specific GMMs for interface subduction zone earthquakes are not yet available for NEI. With this background and considering the high seismic activity of NEI, we developed a GMM for interface subduction zone earthquakes for NEI and its adjacent countries.

2. *Seismotectonics Framework and Historical Seismicity*

The tectonics and geology of NEI and its adjacent countries are complex and seismically active. The seismotectonics map of NEI is shown in Fig. 1a. NEI and its adjoining regions are considered to be the most severe seismic zone in the world (Bora et al. 2016). NEI comprises seven states covering over an

Table 1

Strong motion records for NEI interface subduction earthquakes

Date (yyyy/mm/dd)	Location		Magnitude (M_w)	Focal depth (km)	No. of stations	Dip angle (degrees)	Range (km)
	Latitude (N)	Longitude (E)					
2018/01/07	24.738	94.906	5.6	33	2	27	102–152
2017/01/03	24.015	92.018	5.7	32	8	17	82–240
2014/11/20	23.508	93.515	5.6	49	3	14	96–286
2013/03/02	24.677	92.222	5.2	39	3	23	126–198
2009/09/21	27.332	91.437	6.3	14	2	19	167–274
2007/11/11	22.150	92.388	5.5	29	5	22	214–286
2004/12/09	24.757	92.539	5.4	35	8	32	38–281
2003/07/26	22.854	92.306	5.7	10	2	16	38–155
1997/05/08	24.896	92.254	6.0	35	11	33	37–122
1988/02/06	24.647	91.514	5.8	15	18	29	80–204
1987/05/18	25.271	94.202	5.9	50	14	34	102–248
1986/09/10	25.420	92.080	5.3	43	12	31	50–95

area of 254,979 km^2. In NEI, there are 11 important cities with a population more than 10,00,000.

Goswami and Sharma (1982) and Singh et al. (2016) divided NEI into six tectonic blocks. Of the six tectonic blocks, the Arakan Yoma belt tectonic (AYBT) block is considered a subduction zone in NEI and its adjacent countries (Rahman 2012). The Indian tectonic plate is bounded by four major tectonic plates: the Eurasian Plate in the north, the Australian Plate in the southeast, the African Plate to the southwest and the Arabian Plate in the west. The Indian Plate is moving northward relative to the Eurasian Plate and collides with it. As a result, the Indian Plate is subducted by the Eurasian Plate. The Indo-Burma (Myanmar) subduction boundary is highly oblique to the direction of relative velocity of the Indian Plate with respect to the Eurasian Plate (Satyabala 2003). This area includes features of active subduction zones in NEI such as the Wadati-Benioff zone of earthquakes, a magmatic arc, and thrust and fold belts (Satyabala 2003). The Burmese arc forms the eastern margin of the Indian Plate where the Indian lithospheric slab is subducted eastward beneath the Burmese Plate (Ni et al. 1989).

Two major faults are recognized in the Indo-Burma subduction region, the Kabaw and the Sagaing faults (Fig. 1a). The Kabaw fault (also called the eastern boundary fault) forms a major tectonic break between the Indo-Burma Range (IBR) and the Myanmar Central Basin (MCB), and it continues to the southwest Andaman fault (Nandy 1986). The Kabaw fault forms a boundary between the IBR and MCB, whereas the Sagaing fault separates the Shan Plateau from the MCB (Fig. 1a).

3. *Historical Seismicity of the Region*

NEI and its adjacent countries have experienced several historical large earthquakes (Seebar and Armbruster 1981; Molnar and England 1990; Rahman 2012). It is believed that these earthquakes are associated with subduction in the IBR (Le Dain et al. 1984; Satyabala 2002). Some of the significant historical interface subduction earthquakes in NEI and its adjacent countries are described below.

The Srimangal earthquake occurred on 7 July 1918, and its M_w and focal depth were 7.6 and 14 km, respectively (Fig. 1b; United States Geological Survey (USGS)). The worst affected area was the southern Sylhet District in Bangladesh and its adjoining northern state of Tripura in NEI. The origin of this earthquake was the Sylhet fault (Tiwari 2002).

The Tagaung earthquake (M_w 8.0) occurred on 12 September 1946 in Myanmar with a focal depth of 15 km (Fig. 1b; USGS). Landslides and enormous land fissures developed due to the ground shaking, and a few people were killed. Cracks were observed on the ground in many places. Several buildings and pagodas collapsed in Htichaing, Kawlin, Tagaung

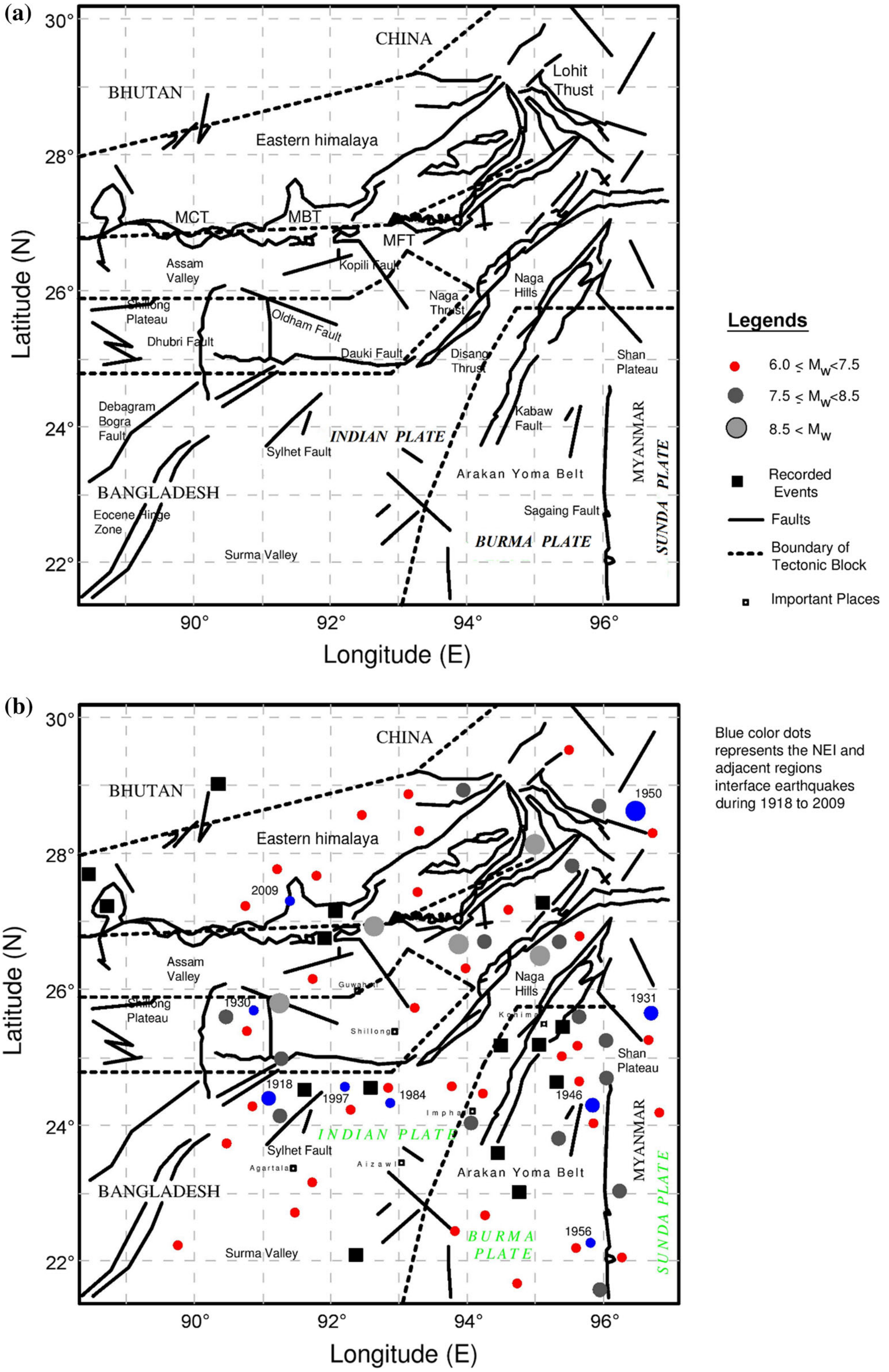

Blue color dots represents the NEI and adjacent regions interface earthquakes during 1918 to 2009

◀Figure 1
a, **b** The tectonic and seismotectonic map of NEI and its adjacent countries. The figure shows NEI interface earthquakes of $M_w \geq 6.0$ and focal depth 10 to 50 km

and Thabeikyn (Aung 2015). The Sagaing fault was assigned as the origin of this earthquake (Aung 2015; Hurukawa and Maung 2011).

One of the most disastrous earthquake (M_w 8.7) in NEI occurred on 15 August 1950. Its focal depth was 29 km (Fig. 1b; USGS). Tremors were felt throughout NEI. During this earthquake, 1520 peoples were killed, and there was mass destruction of property, livestock, buildings and roads. Forty to fifty percent of wildlife perished over the affected areas. Ground fissures and cracks were observed in many places, from which water and sand spouted out, and landslides were reported in many locations. The effects of this earthquake even diverted some rivers in the region (Tiwari 2002). The Po Chu fault was assigned as the causative fault for this earthquake (Ben Menahem et al. 1974; Ni and York 1978).

Aside from the abovementioned earthquakes, several other high-magnitude interface subduction earthquakes have occurred in NEI, including the 1930 Dhubri (M_w 7.1), 1931 Kamaing (M_w 7.6), 1956 Sagaing (M_w 6.8), 1984 Cachar (M_w 6.0) and 2009 Bhutan (M_w 6.3) earthquakes, which are shown in Fig. 1b (USGS; Tiwari 2002; Hurukawa and Maung 2011; Kayal et al. 2010; Aung 2015).

Steckler et al. (2016) suggested that there is a possibility of a magnitude M_w 8.2–9.0 earthquake occurring in NEI and its adjacent countries. With rapid population growth and large infrastructure development in NEI, the region is becoming more and more vulnerable to seismic threats. Considering the past seismicity and high seismic threat of future earthquakes in NEI, it is necessary to conduct seismic hazard mitigation for NEI and its adjacent countries.

4. Data Acquisition

In this study, a database of interface strong motion records for NEI and its adjacent countries was compiled. In total, there are 88 strong motion records for 12 interface earthquakes (Table 1). These strong motion records were compiled from the National Earthquake Information Center (NEIC) (https://www.usgs.gov/products/data-and-tools/real-time-data), COSMOS Virtual Data Center (https://strongmotioncenter.org/vdc/scripts/earthquakes.plx), International Seismological Center (ISC) (http://www.isc.ac.uk/iscbulletin/search/catalogue), Indian Meteorological Department (IMD) (https://seismo.gov.in/MIS/riseq/earthquake), European Mediterranean Seismological Center (EMSC) (https://www.emsc-csem.org/Earthquake/significant_earthquakes.php) and Incorporated Research Institutions for Seismology (IRIS) (http://ds.iris.edu/seismon/zoom/index.phtml?rgn=S_SE_Asia).

5. Ground Motion Simulation Model

5.1. Point-Source Model

Strong motion records are limited for NEI and its adjacent countries. It will be difficult to develop a new ground motion model for this region with these sparse recorded events. Thus, we used Boore's (1983, 2003) stochastic point-source model for simulation of synthetic ground motion data sets to develop our GMM. This model was used by Atkinson and Silva (2000), Iyengar and Raghukanth (2004), Yenier and Atkinson (2014), and Chhangte et al. (2020) for magnitude M_w up to 8.0 and by Singh et al. (2016) up to M_w 8.5.

The point-source stochastic model (Boore 1983, 2003) is presented below.

$$A(f) = CS(f)D(f)P(f)F(f), \qquad (1)$$

where A(f) is the Fourier amplitude spectrum of ground acceleration, C is a scaling factor, S(f) represents the source spectral function (Brune 1970, 1971), $D(f)$ corresponds to the diminution function characterizing the attenuation for the region, $P(f)$ is a filter for shaping acceleration amplitudes beyond a high cutoff frequency (f_m), $F(f)$ represents the site amplification function (Boore 1996) and the $F(f)$ value is unity at a hard rock level.

The widely used source spectral function is the single-corner frequency model of Brune (1970) and can be expressed as

$$S(f) = (2\pi f)^2 M_0/[1 + (f/f_c)^2], \tag{2}$$

where f_c is the corner frequency in Hz and M_0 is the seismic moment in dyne/cm. The relation between f_c and stress drop ($\Delta\sigma$) in bars (Boore 2003) is

$$f_c = 4.9 \times 10^6 V_s(\Delta\sigma/M_0)^{1/3}, \tag{3}$$

where V_S represents shear wave velocity for the specified region in km/s. The diminution factor $D(f)$ can be expressed as (Boore 2003)

$$D(f) = G \exp\left[\frac{-\pi f R}{V_s Q(f)}\right], \tag{4}$$

where G represents the geometric spreading factor and the second term of $D(f)$ represents the anelastic attenuation. The parameter R from Eq. (4) is hypocentral distance in km and $Q(f)$ is the quality factor of the region defined by Boore (2003) which can be expressed as follows

$$Q(f) = Q_0 f^{\eta}, \tag{5}$$

where the scaling constant Q_0 characterizes heterogeneities in the medium and η is related to the seismic activity in the region. Q_0 is the Q value at $f = 1.0$ Hz, and η gives the frequency dependence of $Q(f)$. The parameters Q_0 and η in the above equation are calculated from recorded seismic events.

The high-frequency cutoff filter in the above model (Boore 1983, 2003) is expressed as

$$P(f) = \exp(-\pi\kappa f), \tag{6}$$

where the parameter κ represents the kappa factor to reduce the high-frequency amplitudes above some threshold frequency and characterizes the near-surface attenuation (Anderson and Hough 1984).

The scaling factor (C) is expressed as

$$C = (R\theta\Phi)\frac{2\sqrt{2}}{4\pi\rho V_s}, \tag{7}$$

where the parameter $\langle R_{\theta\Phi}\rangle$ signifies the radiation coefficient averaged over an appropriate range of azimuths and take-off angles, and is assumed to be 0.48–0.64 for shear waves, and ρ represents the density of the earth crust at the focal depth, assumed to be 2.8 g/cm^3 in this study. The coefficient $2\sqrt{2}$ in the above equation is the product of the free-surface site amplification and partitioning of energy in orthogonal directions (Boore 2003).

6. *Input Parameters for the GMM*

In the ground motion simulations, we calculated and fixed the limit of various seismic input parameters suitable for NEI and its adjacent countries; the parameters are presented below:

6.1. *Focal Depth*

In total, there are 12 recorded interface subduction zone earthquake events in NEI and its adjacent countries; the events are presented in Table 1. It is observed from Table 1 that the focal depth for these earthquakes varies from 10 to 50 km (Table 1). Hence, we fixed the range of focal depth from 10 to 50 km for NEI and its adjacent countries in the development of the GMM for interface subduction earthquakes.

6.2. *Site Parameters*

The National Earthquake Hazards Reduction Program (NEHRP) has specified different site classes of A to F based on V_{S30}, the time-averaged shear-wave velocity in the top 30 m. Rahman (2012) studied the site class of the recording stations in NEI and found that most of the recording stations in NEI are of site class C. He estimated the average kappa value as 0.06 ± 0.012 s for this site class based on the past recorded events in NEI. Rahman (2012) also stated that only three recording stations were located in site class E or F, and he calculated the average kappa for these soil sites as 0.08 s. It is not possible to develop a GMM due to scarcity of strong motion records for site class C in NEI or any other site class.

Hence, we developed a GMM corresponding to hard rock level (V_{S30} as 2800 m/s) similar to models developed for the Central and Eastern United States (e.g., Campbell 2003; Atkinson 2004; Tavakoli and Pezeskh 2005). The greatest advantage is that ground motions at a hard rock level (V_{S30} as 2800 m/s) can be scaled to site classes A to F using suitable site coefficients. In NEI, all types of site classes from A to F are available. Therefore, we can used our present model conveniently for all A to F site classes which will be helpful in estimating seismic hazard in the whole region. Site coefficients for all site classes A to D are available for NEI (Singh et al. 2016).

However, information on the kappa for hard rock in NEI is not available. Tavakoli and Pezeshk (2005) estimated that the kappa value at the bedrock level is 0.006 s for eastern North America. Similarly, Campbell (2003) has also calculated kappa value as 0.006 s for eastern North America, appropriate for hard rock corresponding to V_{S30} 2800 m/s. Based on this, the kappa value for the hard rock level is fixed as 0.006 s for NEI in our model for the ground motion simulations based on the assumption that hard rock in NEI and Eastern North America are the same.

6.3. *Geometrical Spreading Factor*

Raghukanth and Somala (2009) studied the modeling of strong motion data both for crustal and subduction zone earthquakes in NEI. They used the following geometrical spreading factor (G) for the Indo-Burma Region (IBR) which is valid for interface subduction zone earthquakes of NEI

$$\begin{aligned} G &= 1/R \qquad \text{for } R < 100 \text{ km} \\ G &= 1/(10\sqrt{R}) \quad \text{for } R > 100 \text{ km}. \end{aligned} \tag{8}$$

Raghukanth and Somala (2009) used Eq. (8) for the geometrical spreading factor for a subduction zone earthquake in NEI, which is also the focus area of this study. Singh et al. (2016) also used the same geometrical spreading factor in Eq. (8) for the crustal earthquakes in NEI.

Based on this study, we used the same geometrical spreading factor of Raghukanth and Somala (2009) and Singh et al. (2016) to develop our GMM for interface subduction zone earthquakes of NEI and its adjacent countries.

6.4. *Quality Factor (Q)*

Quality factor (Q) is a key parameter to develop a stochastically simulated GMM. Q is frequency-dependent and increases with frequency as shown in Eq. (5) (Rahman 2012; Raghukanth and Somala 2009; Mitra et al. 2006). The parameters Q_0 and η in Eq. (5) have a significant impact in the GMM. Generally, a seismically active region has a high η and low Q_0 value, whereas a tectonically stable region has a low η and high Q_0 (Kumar et al. 2005; Singh et al. 2004; Mandal and Rastogi 1998). The Q value gives the shape of the high-frequency spectrum of the Fourier amplitude spectra (FAS) of acceleration (Motezedian and Atkinson 2005; Sokolov et al. 2002; Raoof et al. 1999).

In this study, Q value for each of the strong motion records for the interface events (Table 1) at the various recording stations were calculated separately by applying regression analysis. After substituting all of the terms from Eqs. (2) to (8) into Eq. (1), we can rewrite Eq. (4) as follows

$$\begin{aligned} A(f) &= \frac{\overline{S(f)}}{R}\exp\left(-\frac{\pi f R}{v_s Q(f)}\right) \qquad \text{for } R < 100 \text{ km} \\ A(f) &= \frac{\overline{S(f)}}{10\sqrt{R}}\exp\left(-\frac{\pi f R}{v_s Q(f)}\right) \quad \text{for } R > 100 \text{ km}, \end{aligned} \tag{9}$$

where $\overline{S(f)} = CS(f)P(f)F(f)$.

By taking $\log_{10}$ on both sides of Eq. (9), we obtain

$$\begin{aligned} \log_{10} A(f) + \log_{10} R &= \log_{10}\left(S(f) - \frac{\pi f R \log_{10} e}{v_s Q(f)}\right) \qquad \text{for } R < 100 \text{ km} \\ \log_{10} A(f) + 5\log_{10} R &= \log_{10}\left(S(f) - \frac{\pi f R \log_{10} e}{v_s Q(f)}\right) \qquad \text{for } R > 100 \text{ km}. \end{aligned} \tag{10}$$

The intercept in Eq. (10) is given by the source term $\log_{10} \overline{S(f)}$ and the slope by inverse (*1/Q*) term. For each earthquake, we plot $\log_{10}A(f)$ + (1 or 5)$\log_{10}R$ versus R and perform a linear regression analysis to determine Q at each frequency.

Equation (5) can be rewritten as

$$\log_{10} Q(f) = \log_{10} Q_0 + \eta \log_{10} f. \tag{11}$$

Linear regression is carried out over $\log_{10}Q(f)$ versus $\log_{10}$f to determine the values of Q_0 and η from the intercept and the slope of the regression line, respectively. In this study, the horizontal components (Q_{LT}) value of the quality factor is calculated, which is obtained by taking the average of the longitudinal and transverse components of the recorded strong motion accelerogram.

$\log_{10}A + (1/5)\log_{10}R$ versus R is plotted in Fig. 2a–f for the horizontal components of $Q(f)$ at the frequency of 0.2 Hz for 10 September 1986, 18 May 1987, 6 February 1988, 8 May 1997, 9 December 2004 and 3 January 2017 earthquakes, respectively. This figure illustrates suitable Q results with mean value of $\pm \sigma_1$ (standard deviation). The slope of the line is an estimate of Q at that particular frequency.

The dependence of Q on f is given in Fig. 3a–f for the horizontal components of 10 September 1986, 18 May 1987, 6 February 1988, 8 May 1997, 9 December 2004 and 3 January 2017 earthquakes, respectively. We calculated $Q(f)$ for 12 recorded events which are given in Table 2.

The average of the horizontal component of Q for all 12 interface earthquakes for NEI is calculated as

$$Q_{\mathrm{LT}}(f) = 172.84 f^{0.96}, \qquad (12)$$

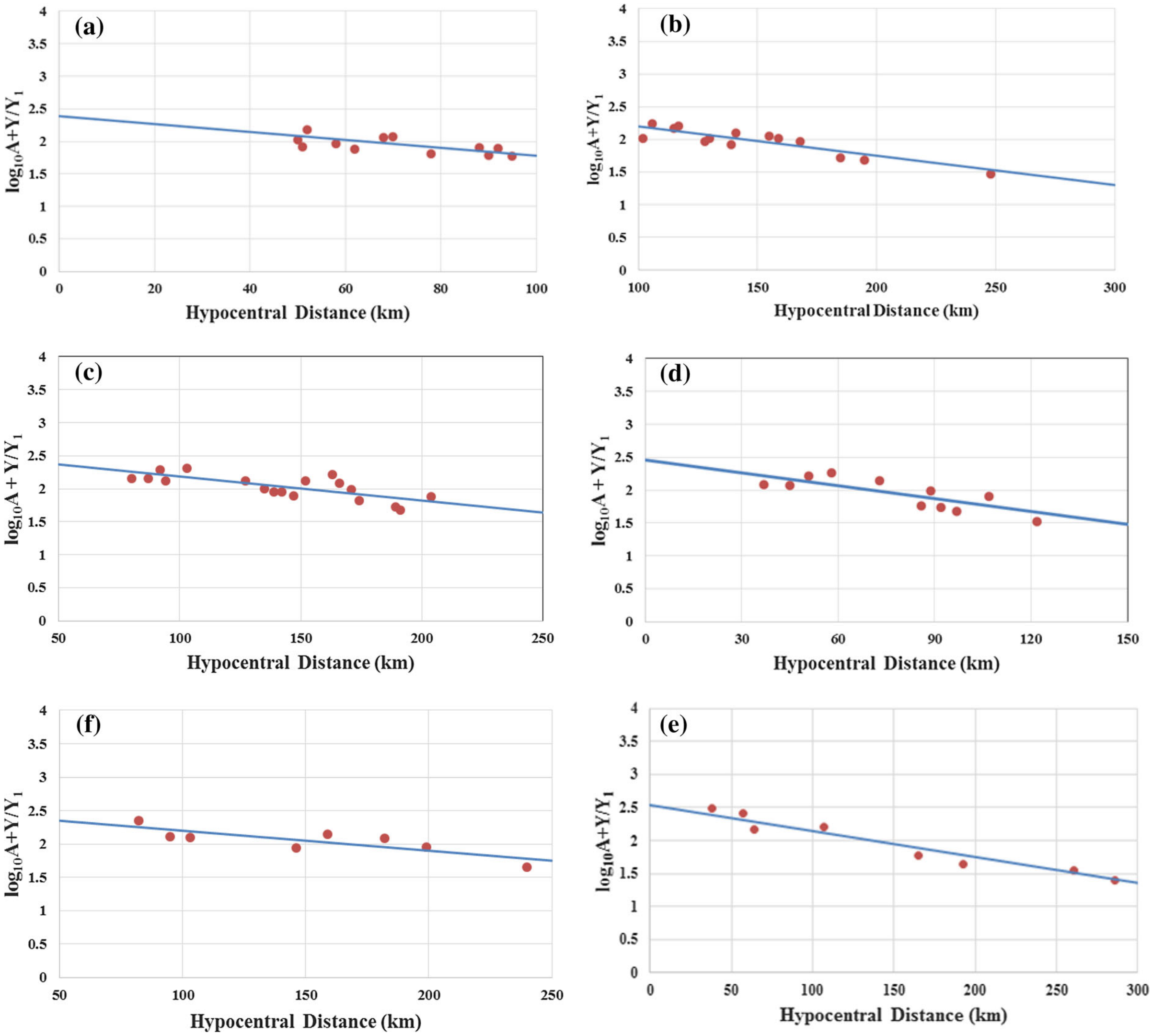

Figure 2

Variation of $\log_{10}A + Y/Y_1$ versus R (km) for the horizontal components at 0.2 Hz for **a** 10 September 1986, **b** 18 May 1987, **c** 6 February 1988, **d** 8 May 1997, **e** 9 December 2004 and **f** 3 January 2017. $Y = \log_{10}R$ ($R < 100$ km) and $Y_1 = 5\log_{10}R$ ($R > 100$ km)

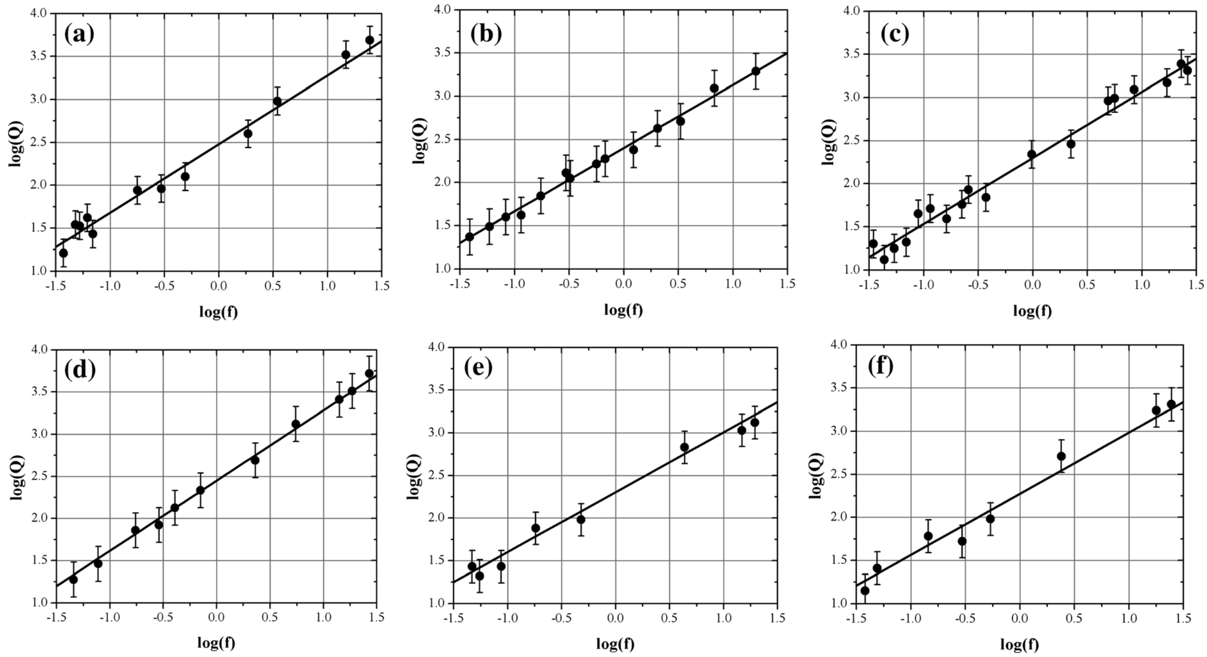

Figure 3

Weighted average of the $\log_{10}Q$ versus $\log_{10}f$ for the horizontal component for **a** 10 September 1986, **b** 18 May 1987, **c** 6 February 1988, **d** 8 May 1997, **e** 9 December 2004 and **f** 3 January 2017

with the standard deviation (σ_1) values as (14.4 (Q_0), 0.042 (η)).

Rahman (2012) calculated the frequency-dependent $Q(f)$ for subduction earthquakes in NEI. He stated that for subduction zone earthquakes in NEI, Q_0 value ranges from 178.59 to 193.50, and η value varies from 0.93 to 0.97. Raghukanth and Somala (2009) also estimated an average $Q(f)$ for NEI subduction zone earthquakes as $Q(f) = (434 \pm 9)f^{(0.72\pm0.01)}$ with standard deviation σ_1 as 0.3, based on four strong motion records in NEI. Mitra et al. (2006) also estimated $Q(f)$ for the Indian platform for a few events applying regression analysis.

Table 2

Calculated quality factor (Q) values for NEI interface subduction earthquakes

Date (yyyy-mm-dd)	Magnitude (M_w)	Horizontal Q (Q_{LT}), (σ_1)
1986-09-10	5.3	$172.56f^{0.92}$, (12, 0.03)
1987-05-18	5.9	$179.63f^{0.97}$, (14, 0.04)
1988-02-06	5.8	$172.34f^{0.99}$, (13, 0.032)
1997-05-08	6.0	$171.21f^{0.92}$, (10, 0.04)
2003-07-26	5.7	$165.6f^{0.93}$, (13, 0.03)
2004-12-09	5.4	$173.6f^{0.96}$, (12, 0.022)
2007-11-11	5.5	$165.77f^{0.92}$, (11, 0.025)
2009-09-21	6.3	$189.66f^{0.97}$, (14, 0.04)
2013-03-02	5.2	$195.87f^{0.98}$, (19, 0.03)
2014-11-20	5.6	$144.5\ f^{0.97}$, (18, 0.05)
2017-01-03	5.7	$141.7f^{0.96}$, (15, 0.045)
2018-01-07	5.6	$164.2f^{0.97}$, (17, 0.05)

We estimated Q for all the strong motion records of interface subduction earthquakes in NEI, which are presented in Table 2. It was observed from the 12 recorded interface subduction zone earthquakes (Table 2), Q_0 value for the interface subduction zone earthquakes in NEI varies from 141 to 196, and η value varies from 0.92 to 0.99.

6.5. *Stress Parameters ($\Delta\sigma$)*

Fourier amplitude spectra (FAS) of ground motion at a site (Boore 1983; 2003) can be expressed from Eq. (1). Hence, stress parameters ($\Delta\sigma$) can be found by substituting Eq. (4) for f_c into $A(f)$ of Eq. (4), and we can get the following expression

$$A(f) = \frac{2\sqrt{}2(2\pi f)^2 M_0(R_{\theta\Phi})}{4\pi\rho V_s^3 1 + \frac{f}{4.9V_s 10^6\left(\frac{\Delta\sigma}{M_0}\right)^{\frac{1}{3}}}^2} G \exp\left(-\frac{\pi f R}{V_s Q(f)}\right) \exp(-\pi k f) F(f), \tag{13}$$

where M_0 is the seismic moment which is calculated as: $\log_{10}(M_0) = 1.5\ M_w + 16.05$ (Hanks and Kanamori 1979).

Strong motion records in NEI are available for 91 frequencies (f) from 0.0667 to 25 Hz. V_s and ρ are the shear-wave velocity (3.6 km/s) and density (2.8 gm/cc) at the bedrock level, respectively, in Eq. (13).

The site amplification function, $F(f)$, for the NEHRP site class C is calculated in the present study for all the 91 frequencies for each recording station with respect to rock using Boore's (1996, 2003) SMSIM Fortran program with the rock kappa factor κ at 0.006 s, shear wave velocity V_s as 580 m/s and κ as 0.0545 s for the site class C recording stations in NEI (Rahman 2012). The site amplification function $F(f)$ for the NEHRP site class C is shown in Fig. 4.

From Eq. (13), for given values of R and 91 frequencies for all the recording stations for a past event in NEI, theoretical Fourier spectral values $A(f)$ are calculated for the various $\Delta\sigma$ values of 10–400 bars. The frequency content of each theoretically calculated Fourier spectrum (TCFS) is compared with the observed Fourier spectrum (OFS). Residuals for all 91 frequencies within a range of 0.0667–25 Hz over all records are calculated for site class C.

By taking averages of all frequencies, the mean square error (MSE) is found from OFS and TCFS as follows

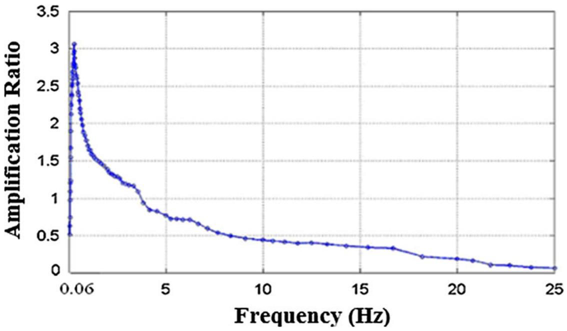

Figure 4
Site amplification function $F(f)$ for NEI interface subduction zone

$$\mathrm{MSE} = \frac{1}{n}\Sigma(\mathrm{OFS} - \mathrm{TCFS})2 \tag{14}$$

where n is the total number of frequencies for all the recording stations for each past event.

The MSE between the recorded OFS and the TCFS is calculated with respect to various $\Delta\sigma$ values using Eq. (14). MSE between the recorded OFS and TCFS is minimized by plotting MSE with respect to $\Delta\sigma$ values. The $\Delta\sigma$ value corresponding to the minimum MSE value is the desired stress factor for the given past earthquake. Equation (14) is valid for estimating stress drop for a particular event in a region as all others source parameters used in Eqs. (16) and (22) are the same in NEI.

We estimated stress parameters for all 12 recorded NEI interface events presented in Table 1. The MSE versus stress drops for the earthquakes on 10 September 1986, 18 May 1987, 6 February 1988, 8 May 1997 earthquakes, 9 December 2004 and 3 January 2017 are presented in Fig. 5a–f, respectively. It is observed that the MSEs are minimum at the $\Delta\sigma$ values of 249, 269, 253, 155, 173 and 181 bars, respectively. For these corresponding stress parameter values, the distributions of residuals at all 91 frequencies with respect to hypocentral distances are shown in Fig. 6a–f for 10 September 1986, 18 May 1987, 6 February 1988, 8 May 1997, 9 December 2004 and 3 January 2017 earthquakes, respectively. It is observed from Fig. 6a–f that the residuals are unbiased with respect to hypocentral distances. The distribution of residual versus hypocentral distance for $\Delta\sigma$ value is plotted in Fig. 6a–f to rule out a trend of residuals with respect to the hypocentral distance.

Rahman (2012) calculated $\Delta\sigma$ for subduction earthquakes in NEI. He stated that for subduction zone earthquakes in NEI, $\Delta\sigma$ values ranges from 124 to 180 bars. Raghukanth and Somala (2009) also estimated $\Delta\sigma$ for subduction zone earthquakes for NEI ranging from 123 to 282 bars.

We estimated $\Delta\sigma$ for all the strong motion records of interface subduction earthquakes in NEI, as presented in Table 3. It is observed from Table 3 that for the interface earthquakes, the $\Delta\sigma$ values vary from 127 to 274 bars. Based on these analyses, we fixed the range of $\Delta\sigma$ values from 110 to 280 bars for the ground motion simulations in Table 4.

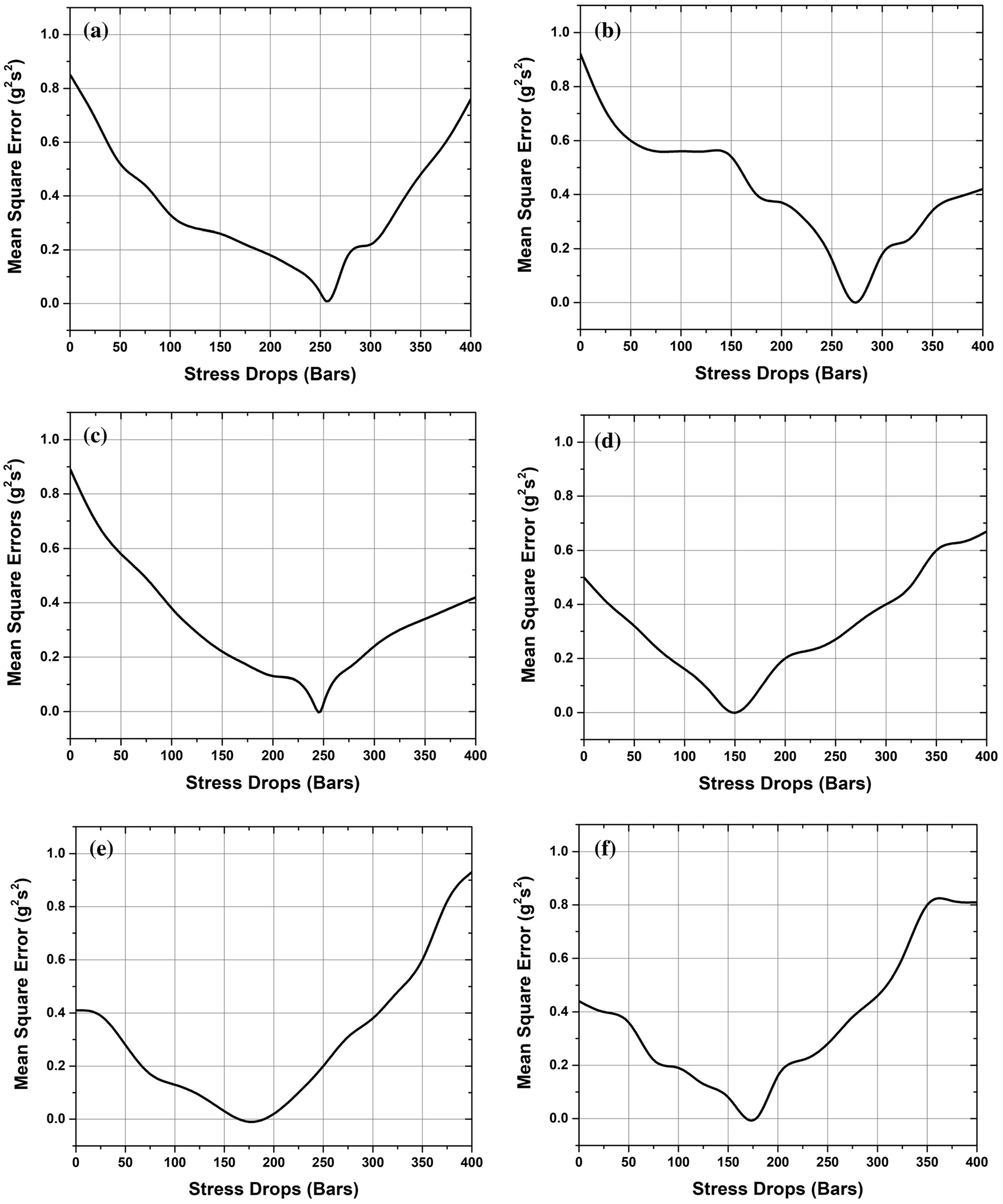

Figure 5
Variation of the MSE with Δσ values for the earthquakes on **a** 10 September 1986, **b** 18 May 1987, **c** 6 February 1988, **d** 8 May 1997, **e** 9 December 2004 and **f** 3 January 2017

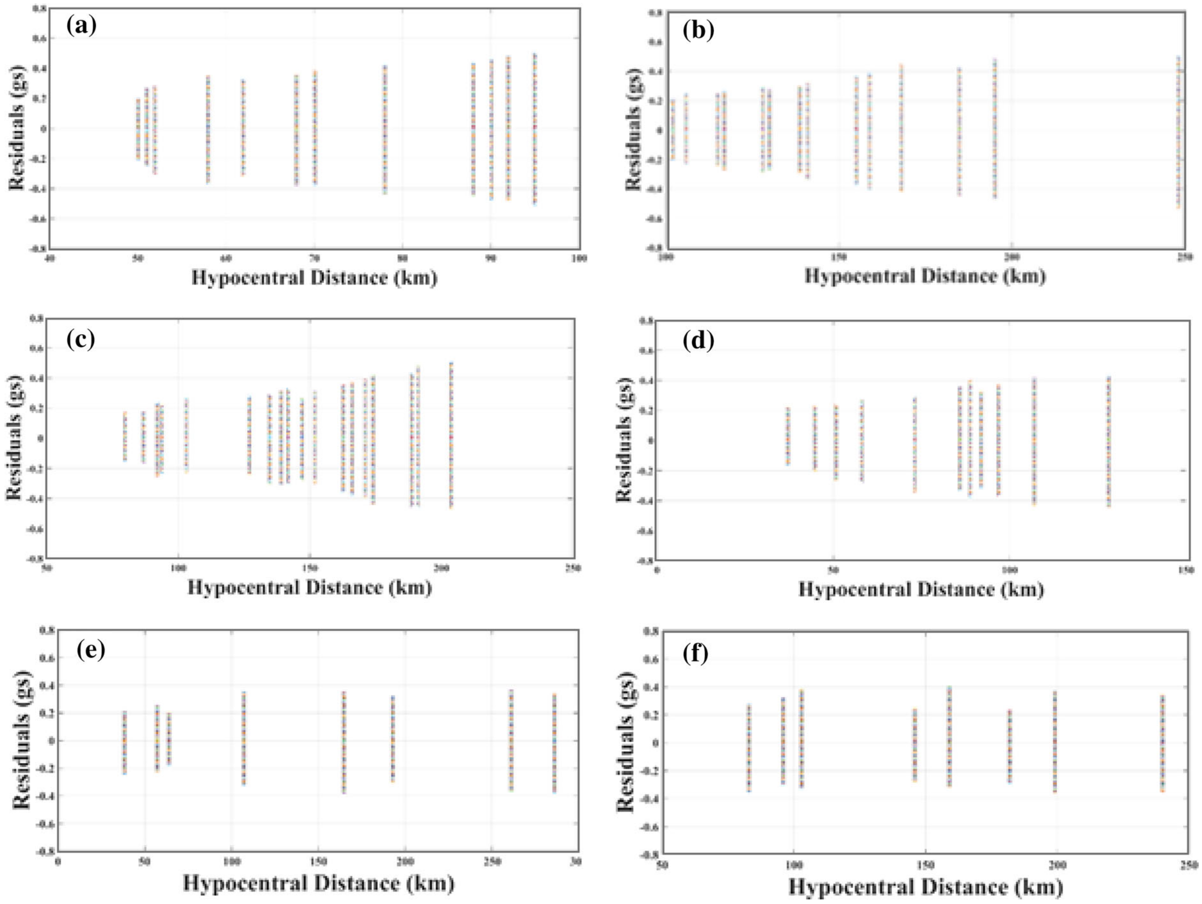

Figure 6
Distribution of the residuals for the calculated $\Delta\sigma$ value of earthquakes on **a** 10 September 1986, **b** 18 May 1987, **c** 6 February 1988, **d** 8 May 1997, **e** 9 December 2004 and **f** 3 January 2017

We applied a bootstrap method to define the uncertainty associated with the attenuation parameters. We randomly selected 90% of these earthquake records, and we duplicated some of the data to keep almost the same amount of total data computed as in the original data set (Singh et al. 2016; Drouet and Cotton 2015). We repeated this operation 150 times, and for each data set, we ran the inversion method of Drouet et al. (2010). Ultimately, we generated 150 sets of parameters from which we can draw distributions that represent the observed variability, which is shown in Fig. 7a, b. The anelastic model parameters obtained using a bootstrap technique are $\log_{10}(Q_0)$ as 2.29 ± 0.17, $\gamma = 0.98 \pm 0.008$ and $\eta = 0.91$–0.99 which are presented in Table 4. Attenuation parameters are not independent, and correlation should be taken into account, but for the simplicity and to remain conservative, we assumed independent attenuation parameters (Drouet and Cotton 2015).

6.6. *Path Duration* (*T_p*)

In ground motion simulation, time duration (T_d) also plays an important role (Boore 2003), and it is defined as the sum of a source duration (T_s) and path duration (T_p) in addition to the other effects related to different site conditions or complex source effects such as directivity (Kempton and Stewart 2006). In the present study, we estimated T_p using both the acceleration and velocity database of interface earthquakes of NEI applying two criteria, 5–75% and 5–95% of total energy (Singh et al. 2016). We

Table 3

Calculated stress drop ($\Delta\sigma$) values for NEI interface subduction earthquakes

Date (yyyy-mm-dd)	Latitude (N)	Longitude (S)	Magnitude (M_w)	Stress drop (bars)
1986-09-10	25.420	92.080	5.3	256
1987-05-18	25.271	94.202	5.9	274
1988-02-06	24.647	91.514	5.8	247
1997-05-08	24.896	92.254	6.0	148
2003-07-26	22.854	92.306	5.7	127
2004-12-09	24.757	92.539	5.4	175
2007-11-11	22.150	92.388	5.5	139
2009-09-21	27.332	91.437	6.3	243
2013-03-02	24.677	92.222	5.2	261
2014-11-20	23.508	93.515	5.6	225
2017-01-03	24.015	92.018	5.7	178
2018–01-07	24.738	94.906	5.6	179

Table 4

Ranges of ground motion input model parameters

Parameters	Distribution	Range
Cutoff frequency	Uniform	20–50 Hz
Radiation coefficient	Uniform	0.48–0.64
Focal depth	Uniform	10–50 km
Stress parameter	Uniform	110–280 bars
Attenuation model	Uniform	$\log_{10}(Q_0) = 2.29 \pm 0.17$ $\gamma = 0.98 \pm 0.008$ $\eta = 0.91 - 0.99$
Time duration model	Uniform	$R(16.5/60)$, if $R < 60$ km $16.5 + 0.05\ (R - 60)$, if $R \geq 60$ km
Kappa	–	0.006 s

computed the integral of the square acceleration and velocity within a time window from the shear-wave onset and the shear-wave onset plus 50 s (Drouet and Cotton 2015; Singh et al. 2016). We deducted the source duration ($1/f_c$) to obtain the value of path duration.

It is observed that the path durations computed from 5 to 75% energy criteria are shorter than those obtained from 5 to 95% energy criteria. It is observed from Fig. 8 that a two-segment linear model is best fitted over an average data per distance bin, with a kink point of 60 km for 5–75% energy criteria and more than 60 km for 5–95% energy criteria.

The consistency between the input and output path duration is checked based on Drouet and Cotton (2015) and Singh et al. (2016) for different sets of magnitude M_w 5.0–9.0 and distance 30–300 km. We found that the output path duration is equal to 0.92–0.95 times the input path duration based on the consistency of the actual strong motion records for interface earthquakes of NEI. So we adjusted our input model based on 5–95% energy criteria by 1.05 based on Drouet and Cotton (2015) and Singh et al. (2016). Our results compare well to the results obtained by Drouet and Cotton (2015) and Singh et al. (2016).

The final path duration model for NEI based on strong motion records of interface earthquakes is presented below and also shown in Fig. 8:

$$\begin{aligned} T_p &= R(16.5/60) \qquad [R < 60\ \text{km}] \\ T_p &= 16.5 + 0.05(R - 60) \quad [R \geq 60\ \text{km}]. \end{aligned} \tag{15}$$

The ranges of seismic input parameters used for the ground motion simulations for interface earthquakes in NEI and its adjacent countries are presented in Table 4.

After estimating the region-specific seismic input parameters based on the past NEI interface strong motion records and its adjacent countries, ground motions are simulated for a smaller range of M_w (4.5–6.5) and hypocentral distance (30–300 km) corresponding to V_{S30} as 2800 m/s using Boore's (1983, 2003) point-source model. In total, there are 500 scenario pairs of magnitude and distance bins from which 50,000 ground motions are simulated for smaller magnitude to develop the GMM for NEI interface earthquakes and its adjacent countries. For each scenario, 100 sets of ground motions are simulated and presented in Table 5 (Iyengar and Raghukanth 2004; Singh et al. 2016).

6.7. *Finite-Fault Model*

For finite-fault model simulations, a fault is divided into N number of sub-faults ($N = n_l * n_w$, n_l and n_w are the sub-faults along the fault's length and width, respectively). The respective sub-faults are each treated as point-source seismological models. In this study, we used Boore's (1983, 2003) model for

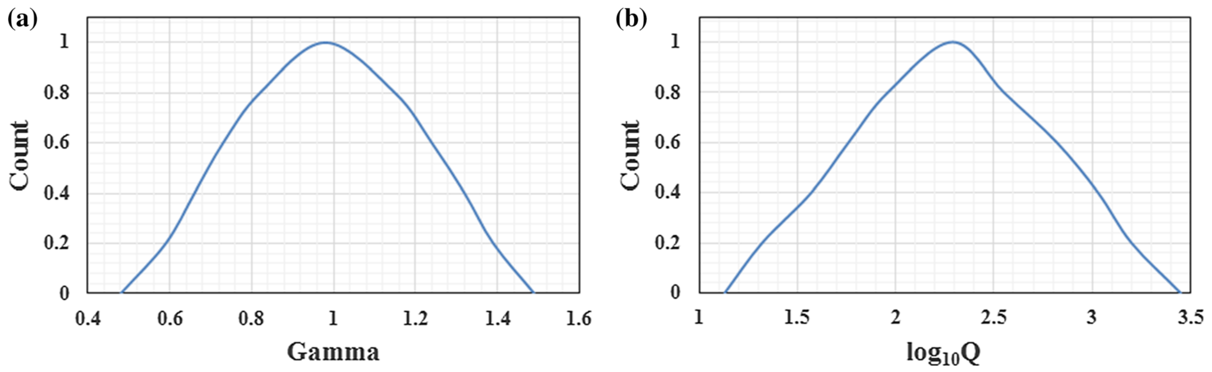

Figure 7
Distribution of the attenuation parameters for NEI interface earthquakes after applying a bootstrapping method to the results and associated Gaussian models: **a** γ and **b** $\log_{10}(Q_0)$

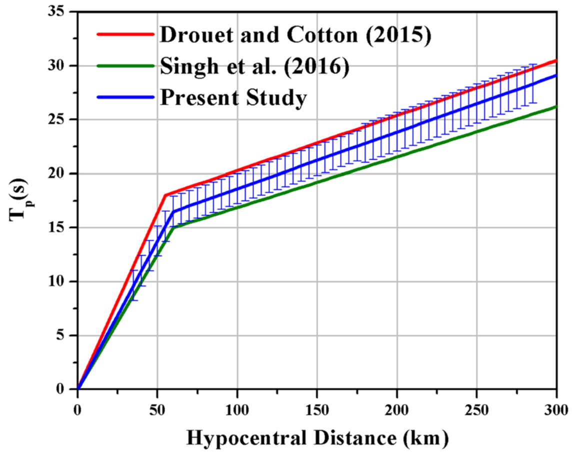

Figure 8
Path component of the duration of shaking (T_p) from NEI interface earthquakes. The present study is compared with Drouet and Cotton (2015) and Singh et al. (2016) for French Alps and NEI crustal earthquakes, respectively. Error bars represent the standard deviation

Table 5

Magnitude and ranges of hypocentral distance for NEI interface earthquakes

Moment magnitude, M_w	Hypocentral distance, R (km)	No. of distance samples	No. of samples
4.5	30–300	100	10,000
5.0	30–300	100	10,000
5.5	30–300	100	10,000
6.0	30–300	100	10,000
6.5	30–300	100	10,000
Total no. of samples			50,000

the analysis, which is shown later. The acceleration spectrum of each sub-fault is modeled as a point source with ω^2 frequency shape (Brune 1970, 1971; Boore 1983, 2003). For the finite-fault simulation, the Fourier amplitude spectrum for each of the ijth sub-faults is replaced by $A_{ij}(f)$, f_{0ij}, R_{ij} and M_{0ij}, where they are the acceleration spectrum of shear wave, corner frequency, hypocentral distance and the seismic moment of the ijth sub-faults. The corner frequency of the sub-fault is given as (Motezedian 2006):

$$\begin{aligned} f_{0ij} &= 4.9\times 10^6 \beta \left(\frac{\Delta\sigma}{M_{0\mathrm{ave}}}\right)^{1/3} \\ &= 4.9\times 10^6 N^{1/3} \beta \left(\frac{\Delta\sigma}{M_0}\right)^{1/3}, \end{aligned} \tag{16}$$

where $M_{0\mathrm{ave}}$ (dyne/cm) is the average seismic moment of the ijth sub-fault.

For identical sub-faults, the sub-fault moment is influence by the ratio of sub-fault area to the total fault area ($M_{0ij} = M_0/N$, M_0 being the total fault moment). If there are nonidentical sub-faults, each sub-fault's seismic moment is given as (Beresnev and Atkinson 1998a, b; Motezedian and Atkinson 2005)

$$M_{0ij} = \frac{M_0 S_{ij}}{\sum_{l=1}^{nl}\sum_{k=1}^{nw} S_{ki}}, \tag{17}$$

where S_{ij} is the relative slip weight of the ijth sub-fault. The sub-fault's ground motions are then summed up in a time domain to obtain spectral acceleration of the entire fault, $A(t)$

Table 6

Events and finite-fault modeling parameters

Date (yyyy/mm/dd)	Magnitude (M_w)	Strike (degrees)	Dip (degrees)	Fault size (km × km)	Sub-fault size (km)	Radiation strength factor
2018/01/07	5.6	210	27	3.9 × 3.9	0.8	1.1
2017/01/03	5.7	147	17	4.5 × 4.5	0.9	1.3
2014/11/20	5.6	156	14	3.9 × 3.9	0.8	1.2
2013/03/02	5.2	329	23	2.2 × 2.2	0.4	0.9
2009/09/21	6.3	27	19	10.9 × 10.9	2.2	1.6
2007/11/11	5.5	251	22	3.4 × 3.9	0.7	1.2
2004/12/09	5.4	243	32	2.9 × 2.9	0.6	1.1
2003/07/26	5.7	2	16	4.5 × 4.5	0.9	1.1
1997/05/08	6.0	78	33	7.0 × 7.0	1.4	1.3
1988/02/06	5.8	239	29	5.2 × 5.2	1.0	1.2
1987/05/18	5.9	67	34	6.1 × 6.1	1.2	1.4
1986/09/10	5.3	156	31	2.5 × 2.5	0.5	0.9

$$A(t) = \sum_{i=1}^{nl} \sum_{j=1}^{nw} A_{ij}\left(t + \Delta t_{ij}\right), \tag{18}$$

where Δt_{ij} is the relative time delay for the radiated wave from the *ij*th sub-fault to reach the observation point. This approach was implemented in the FINSIM (stochastic FINite fault SIMulation; Beresnev and Atkinson 1998a) in the calculation of corner frequency and seismic moment of each sub-fault.

The dimensions of each fault located in NEI and its adjacent regions are calculated based on Strasser et al. (2010). Region-specific seismic input parameters of NEI are used in the program FINSIM for finite-fault model and presented in Tables 6 and 7, respectively. We used 95 numbers of total points for the regression analysis (Strasser et al. 2010).

In finite-fault modeling for NEI, we used the following equation to estimate the size of the sub-fault valid for interface subduction earthquakes (Strasser et al. 2010);

$$Mw = a_1 + b_1 \times \log_{10}(L), \tag{19}$$

$$Mw = a_2 + b_2 \times \log_{10}(W), \tag{20}$$

$$Mw = a_3 + b_3 \times \log_{10}(A), \tag{21}$$

where *L, W* and *A* are the length, width and area of the fault, respectively. The constants a_1 to a_3 and b_1 to b_3 are regression coefficients in Eqs. (19)–(21) calculated by Strasser et al. (2010) for interface subduction earthquakes; they are presented in Table 8.

We simulated higher-magnitude earthquakes for M_w (6.5–9.0) using finite-fault modeling. In this study, the regression coefficients in Eqs. (22–24) are calculated by combining 50,000 simulated data points based on a point-source model and the simulated data obtained from finite-fault modeling for higher-magnitude earthquakes of M_w (6.5–9.0).

6.8. *Ground Motion Model for a Subduction Zone at a Hard Rock Level*

Ground motion parameters are dependent on the magnitude (M_w), hypocentral distance (R) and others region-specific seismic parameters. We adopted the following functional GMM form used by Abrahamson et al. (2016) for global interface subduction earthquakes.

$$\ln(S_a) = \theta_1 + \theta_4 \Delta C_1 + (\theta_2 + \theta_3(M_w - 7.8))\ln(R + C_4 \exp(\theta_7(M_w - 6))) + \theta_6 R + f_{mag}(M_w) + \theta_{10} + f_{site}(PGA_{1000}, V_{S30}), \tag{22}$$

where θ_1–θ_{11} = regression coefficients.

For NEI, $F_{FABA} = 0$ considering NEI as an unknown site.

$$f_{mag}(M_w) = \begin{cases} \theta_4(M_w - (C_1 + \Delta C_1) + \theta_9(10 - M_w)^2 & \text{for} M_w \le C_1 + \Delta C_1 \\ \theta_5(M_w - (C_1 + \Delta C_1) + \theta_9(10 - M_w)^2 & \text{for} M_w > C_1 + \Delta C_1 \end{cases}, \tag{23}$$

Table 7

Generic modeling parameters for NEI interface earthquakes

Parameters	Parameter value
Quality factor	$171.21f^{0.92}$
Geometric spreading	$G = 1/R$ for $R < 100$ km $G = 1/(10\sqrt{R})$ for $R > 100$ km
Path duration model	$\mathrm{TP} = R \times (16.5/60)$ [$R < 60$ km] $\mathrm{TP} = 16.5 + 0.05 \times (R - 60)$ [$R \geq 60$ km]
Crustal amplification	Singh et al. (2016)
Kappa	0.006 s
Stress parameters	180 bars
Window functioning	Saragoni-Hart (Beresnev and Atkinson 1999)
Crustal shear wave velocity	3.6 km/s (Singh et al. (2016)
Rupture velocity	0.8 × Shear wave velocity (Beresnev and Atkinson 1999)
Crustal density	2.8 g/cc (Singh et al. 2016)
Fault-slip distribution	Uniform
Stochastic trial	3 (Beresnev and Atkinson 1999)

Table 8

Regression relations between rupture dimensions and moment magnitude, the multiple determination coefficient (R^2) and total numbers of regression points (N) for interface subduction earthquakes (Strasser et al. 2010), where S.E. is the standard deviation of the coefficient under consideration

Sl. no.	a	S.E. (a)	b	S.E. (b)	σ	R^2	N
1	4.868	0.141	1.392	0.277	0.277	0.814	95
2	4.410	0.277	1.805	0.392	0.392	0.634	85
3	4.441	0.179	0.846	0.286	0.286	0.805	85

where $C_1 = 7.8$. The values of $\varDelta C_1$ are period-dependent variations based on the size of the earthquake.

$$f_{\mathrm{site}}(PGA_{1000}, V_{S30}) = \left\{\theta_8 Ln\left(\frac{V_s}{V_{\mathrm{lin}}}\right) - bLn(\mathrm{PGA}_{1000} + c)\right.$$

$$\left. + bLn\left(\mathrm{PGA}_{1000} + c\left(\left(\frac{V_s}{V_{\mathrm{lin}}}\right)^n\right)\right)\right\} \quad (\text{for } V_{S30} < V_{\mathrm{lin}})$$

or

$$\left\{\theta_8 Ln\left(\frac{V_s}{V_{\mathrm{lin}}}\right) + bnLn\left(\frac{V_s}{V_{\mathrm{lin}}}\right)\right\} \quad (\text{for } V_{S30} \geq V_{\mathrm{lin}}). \tag{24}$$

Here, $V_{S30} = 2800$ m/s.

The regression coefficients in Eq. (22) are presented in Tables 9 and 10.

Table 9

Fixed regression coefficients for (S_a/g) at 5% damping

Coefficient	Value
n	1.0148
c	1.6168
θ_3	0.086
θ_4	0.828
θ_5	0
θ_7	0.368
C_4	9.2

The regression coefficients θ_1–θ_{11} are calculated using a two-stage regression method (Joyner and Boore 1981) to minimize the errors in calculating regression coefficients. Sensitivity analysis is also carried out to check the errors for the various seismic input parameters used in this model.

Site coefficient (FS) for all sites classes can be expressed as follows (Iyengar and Raghukanth 2004; Singh et al. 2016)

$$\ln(F_s) = a_1 Y_{\mathrm{br}} + a_2 + \ln(\sigma_s), \tag{25}$$

where Y_{br} is the bed rock acceleration and σ_s are the standard deviations which were already calculated for NEI for site classes A to D (Singh et al. 2016).

In Eq. (25), a_1 and a_2 are the regression coefficients, which are calculated for all site classes for NEI by Singh et al. (2016) for different time periods. We scaled these site coefficients to the regression coefficients in Tables 9 and 10 for different time periods in conversion to site classes A to D with respect to bed rock acceleration (Singh et al. 2016). Accordingly, we used the site coefficient factors in conversion from hard rock level to site class C in our GMM.

7. *Sensitivity Analysis*

In this paper, the GMM for the NEI subduction zone earthquakes is developed on hard rock level corresponding to V_{S30} of 2800 m/s. Our prediction equation is dependent on the various region-specific seismic input parameters (Table 4). To date, we cannot predict the exact location and specific time of occurrence of earthquakes as they are random in

Table 10

Variable regression coefficients for (S_a/g) at 5% damping

Period	V_{lin}	b	θ_1	θ_2	θ_6	θ_8	θ_9	θ_{10}	θ_{11}
0.000	735.3	−1.127	3.6052	−1.154	−0.0011	0.8289	−0.0116	0.9542	−0.962
0.020	735.3	−1.279	3.6051	−1.153	−0.0011	0.8289	−0.0116	0.9542	−0.981
0.050	895.5	−1.397	3.8664	−1.194	−0.0011	1.0985	−0.0116	1.0463	−1.134
0.075	922.8	−1.543	4.3015	−1.236	−0.0011	1.2593	−0.0120	1.2065	−1.292
0.100	877.6	−1.834	4.5036	−1.236	−0.0011	1.3742	−0.0124	1.2423	−1.293
0.150	746	−2.079	4.6502	−1.221	−0.0012	1.6009	−0.0129	1.1954	−1.238
0.200	636	−2.238	4.4931	−1.194	−0.0016	1.7726	−0.0137	1.1584	−1.196
0.250	556.2	−2.367	4.2980	−1.151	−0.0022	1.9019	−0.0146	1.0878	−1.112
0.300	504.9	−2.498	4.1162	−1.104	−0.0026	2.0236	−0.0156	0.9861	−1.004
0.400	432.6	−2.509	3.8413	−1.017	−0.0033	2.0897	−0.0176	0.7531	−0.735
0.500	392.7	−2.443	3.4683	−0.931	−0.0042	2.0684	−0.0198	0.6211	−0.583
0.600	370.1	−2.281	3.0998	−0.849	−0.0048	1.9557	−0.0219	0.5463	−0.474
0.750	357.1	−1.857	2.7982	−0.791	−0.0056	1.7364	−0.0258	0.4469	−0.321
1.000	348	−0.974	2.4412	−0.742	−0.0061	1.2793	−0.0317	0.3072	−0.137
1.500	348	−0.284	1.7483	−0.674	−0.0062	0.3557	−0.0428	0.2889	−0.846
2.000	348	−0.143	1.2304	−0.619	−0.0062	−0.3492	−0.0532	0.2767	−0.467
2.500	340	−0.086	0.8584	−0.577	−0.0061	−0.6220	−0.0612	0.2765	−0.201
3.000	340	−0.019	0.5546	−0.551	−0.0060	−0.5797	−0.0687	0.2764	0.000
4.000	340	0.000	0.0566	−0.500	−0.0060	−0.5396	−0.0805	0.2736	0.000
5.000	340	0.000	−0.3982	−0.465	−0.0059	−0.5130	−0.0844	0.2734	0.000

nature. Hence, the physics and occurrence of earthquakes are dependent on various input parameters which uncertain. To address this issue, in our model, we considered all these input parameters as uniform distribution (Iyengar and Raghukanth 2004; Singh et al. 2016). Our GMM is based on the ground motion simulations, and it will widely vary depending on the variation of these input parameters. Based on this, sensitivity analysis was performed to check the bias of the GMM corresponding to individual seismic input parameters. After performing the sensitivity analysis, we considered necessary precautionary measures in selecting the input parameters for our model.

In the sensitivity analysis, we checked the impact of the different parametric uncertainties in our model. We performed a sensitivity analysis for focal depth, cutoff frequency, stress drop, radiation pattern, anelastic attenuation, geometric attenuation and time duration. Finally, in our model, total uncertainties were checked by sensitivity analysis.

In the sensitivity analysis, we calculated the standard deviation of our model for each input parameter for different spectral periods and obtained the highest value of standard deviation that can occur in the model (Table 11). Drouet and Cotton (2015) also performed their French Alps GMM sensitivity analysis on empirical models for Europe and Japan, and stochastic models for the United Kingdom and Switzerland. Singh et al. (2016) carried out sensitivity analysis for NEI to check the bias of their model developed for crustal earthquakes in NEI. Based on their study, they concluded that standard deviations spread considerably from 0.6 to 1.0 in natural

Table 11

Estimated standard deviation of the model parameters in sensitivity analysis

Serial no.	Model uncertainty parameters	Standard deviation (ln)
1	Focal depth	± 0.10
2	Cutoff frequency	± 0.09
3	Stress drop	± 0.12
4	Radiation pattern	± 0.05
5	Anelastic attenuation	± 0.17
6	Geometric attenuation	± 0.15
7	Time duration	± 0.10
8	κ (kappa)	± 0.45
9	Site coefficient	± 0.52
10	Total uncertainties	± 0.71

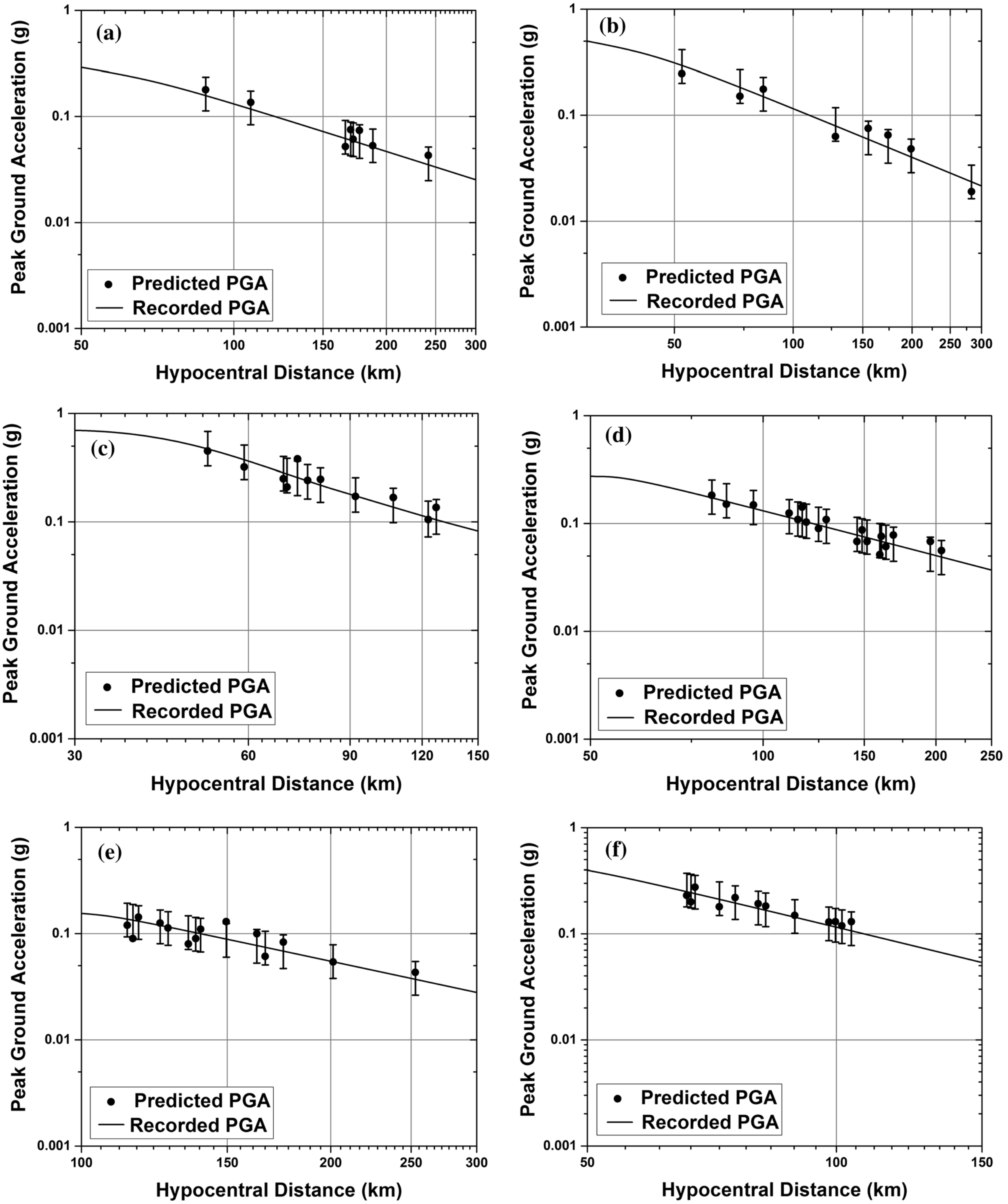

Figure 9
Predicted and recorded PGA values at site class C for **a** M_w 5.7 on 3 January 2017, **b** M_w 5.4 on 9 December 2004, **c** M_w 6.0 on 8 May 1997, **d** M_w 5.8 on 6 February 1988, **e** M_w 5.9 on 18 May 1987, and **f** M_w 5.3 on 10 September 1986. Error/vertical bar represents the standard deviations of the GMM

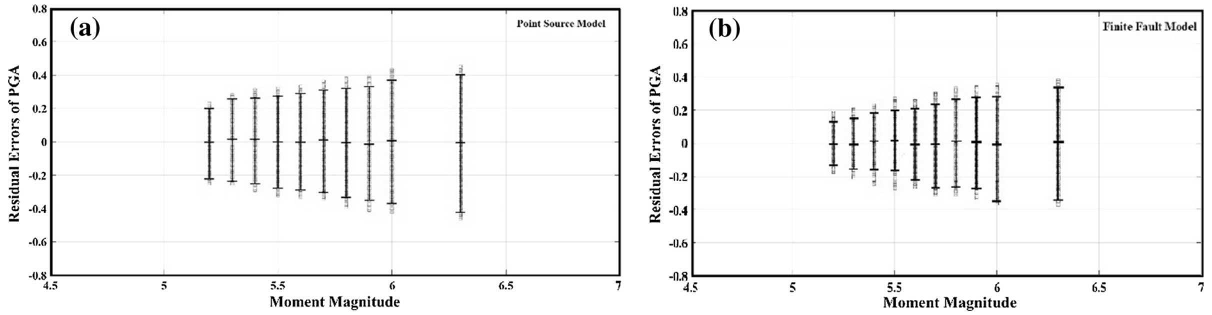

Figure 10
Distribution of PGA residuals with respect to M_w for **a** point-source and **b** finite-fault models. Here, the residuals for each earthquake event are shown with a black vertical line with three horizontal bars showing the ranges of average ± standard deviations of residuals

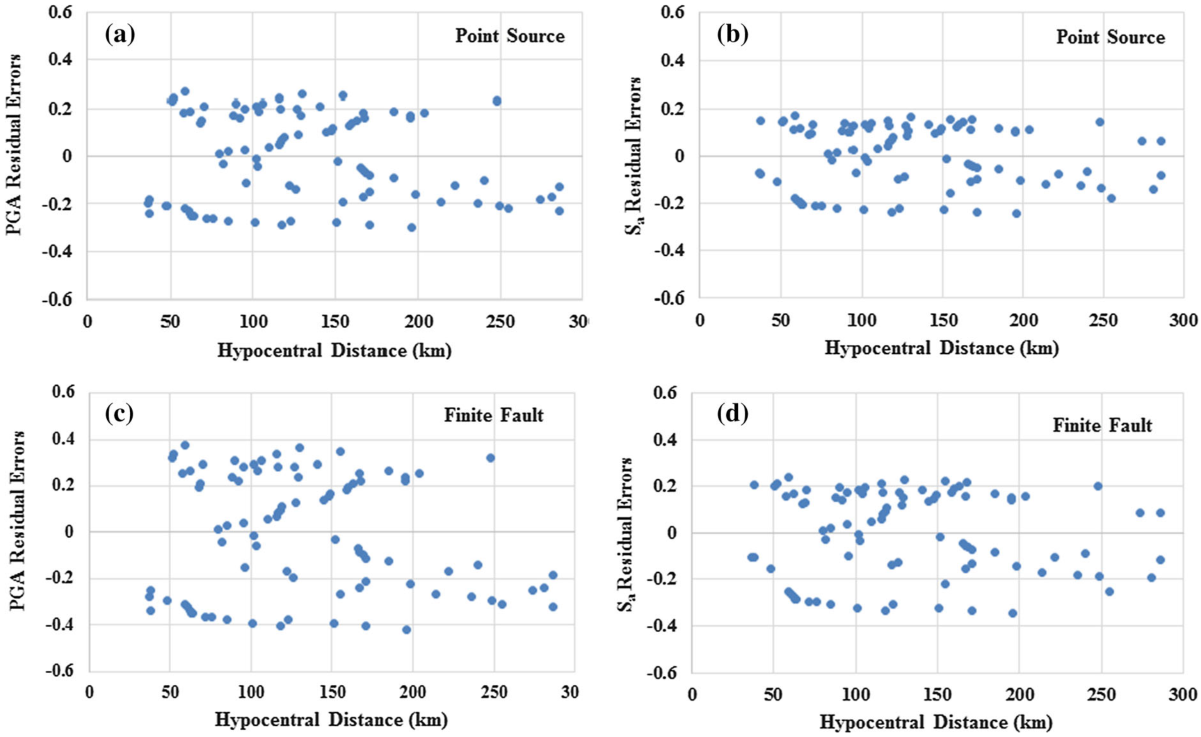

Figure 11
Distribution of the residuals of **a** PGA, **b** 2.0-s S_a for a point-source model; **c** PGA, **d** 2.0-s S_a for a finite-fault model with respect to hypocentral distance (km)

logarithm units. In our model, the spread of standard deviations for the input parameters varied from 0.05 to 0.52 (Table 11). It is observed from Table 11 that standard deviations due to the input parameters, namely focal depth, cutoff frequency, stress drop, radiation pattern, anelastic attenuation, geometric attenuation and time duration, are very small. This indicates that our model is not biased with respect to these region-specific input parameters. We neglected the uncertainty of site coefficient and κ value in the sensitivity analysis in our model. Variation of standard deviations will be large if we considered two input parameters such as site amplification and κ value in the sensitivity analysis. Therefore, we treated

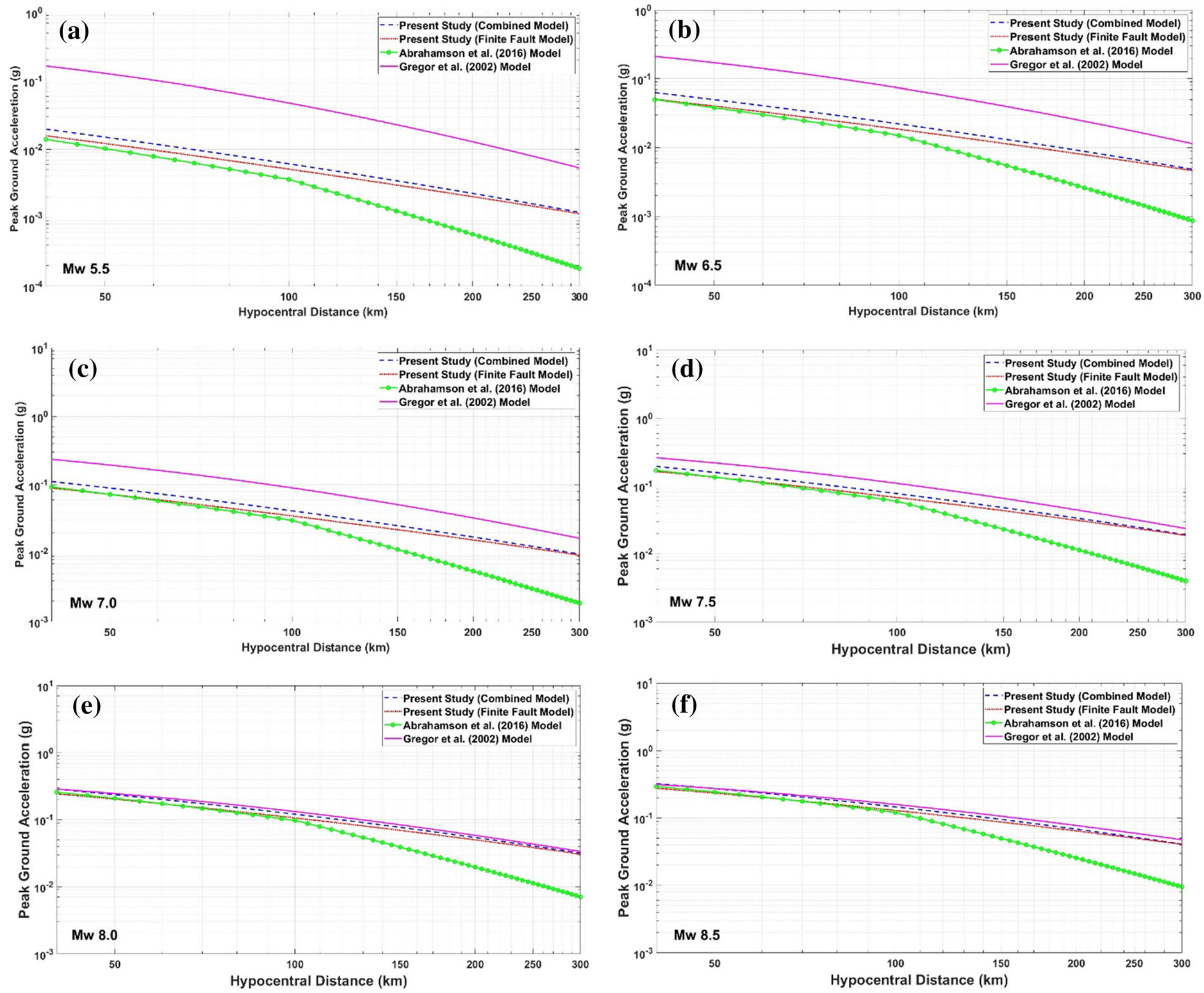

Figure 12

Comparison of peak ground acceleration of the present GMM (point- source and finite-fault model) with Gregor et al.'s (2002) and Abrahamson et al.'s (2016) for M_w **a** 5.5, **b** 6.5, **c** 7.0, **d** 7.5, **e** 8.0 and **f** 8.5 w.r.t. hypocentral distance (km), respectively

these two uncertainties separately. We fixed the value of kappa as 0.006 s. We also used the site effects coefficients calculated by Singh et al. (2016) for NEI in our GMM.

8. *Comparison with Other GMMs*

A GMM for interface subduction zone earthquakes for NEI and its adjacent countries has not yet been developed. Thus, to validate our GMM, we checked our model with the available recorded site class C events and also compared it with Gregor et al.'s (2002) GMM for Cascadia megathrust interface earthquakes and Abrahamson et al.'s (2016) global interface earthquakes.

Our GMM is developed on a hard rock level corresponding to V_{S30} = 2800 m/s which is scaled to site class C ($V_{S30} \approx$ 400 to 500 m/s) using site coefficients calculated by Singh et al. (2016). Gregor et al. (2002) developed a GMM corresponding to average $V_{S30} \approx$ 363 m/s which is also categorized as site class C. Abrahamson et al. (2016) developed a GMM as a function of V_{S30}, and we used Abrahamson et al.'s (2016) model corresponding to average

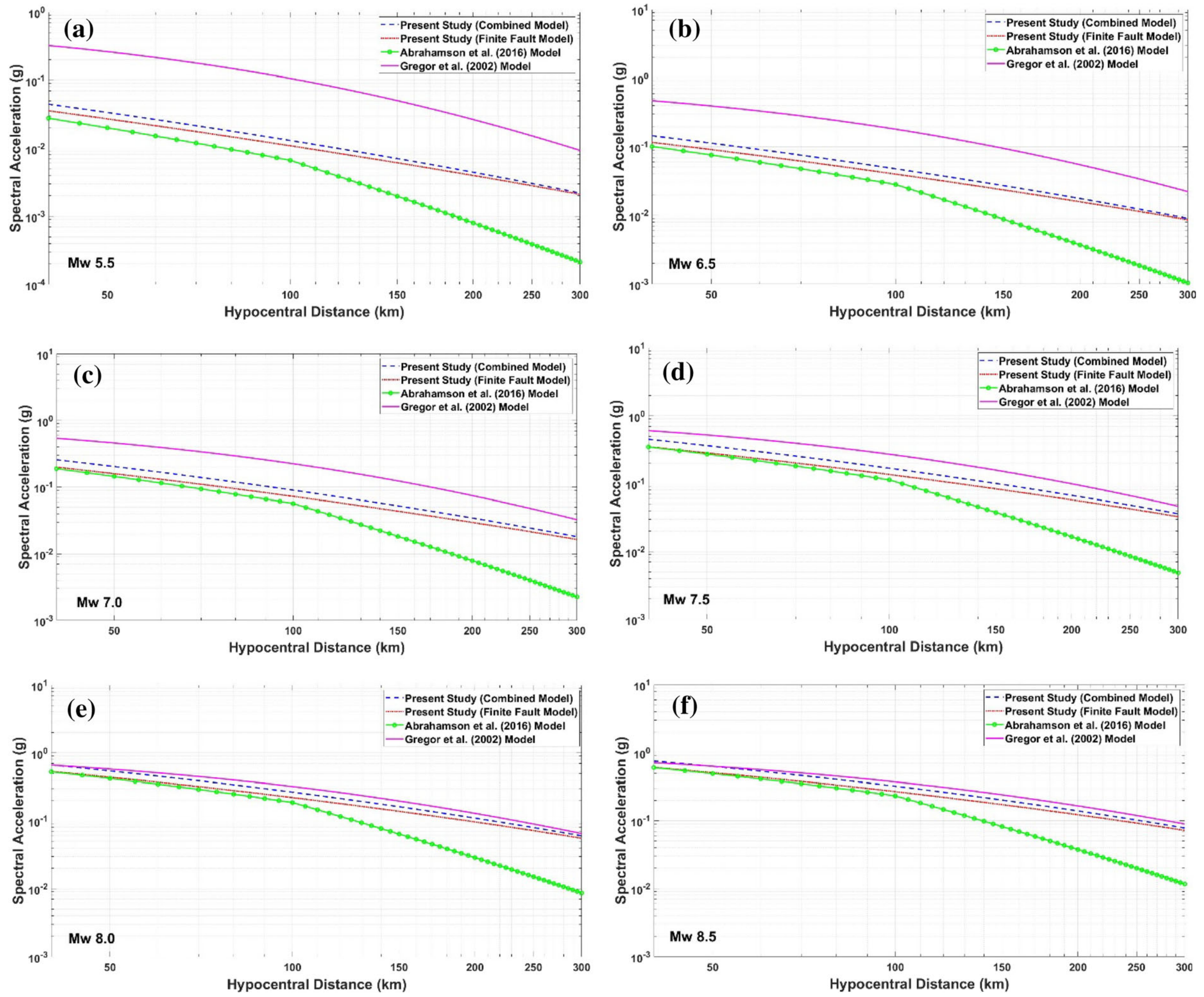

Figure 13

Comparison of spectral acceleration of the present GMM (point-source and finite-fault model) with Gregor et al.'s (2002) and Abrahamson et al.'s (2016) for M_w **a** 5.5, **b** 6.5, **c** 7.0, **d** 7.5, **e** 8.0 and **f** 8.5 at 0.2 s w.r.t. hypocentral distance (km), respectively

$V_{S30} \approx 560$ m/s for site class C in our GMM comparison.

In this study, we checked our model for the interface subduction zone earthquakes with the strong motion records for M_w 5.7 on 3 January 2017, M_w 5.4 on 9 December 2004, M_w 6.0 on 8 May 1997, M_w 5.8 on 6 February 1988, M_w 5.9 on 18 May 1987 and M_w 5.3 on 10 September 1986 in Fig. 9a–f, respectively. It is observed from Fig. 9a–f that our model is not biased with respect to both magnitude and hypocentral distance. We evaluated residuals, mean residuals ± standard deviation for peak ground acceleration (PGA) with respect to magnitude which is shown in Fig. 10a, b based on point-source and finite-fault simulation models. From Fig. 10a, b, it is observed that residuals for PGA are not biased for all ranges of magnitude for both simulation models. We also computed residuals for PGA and spectral acceleration (S_a) at 2.0 s using a point-source model with respect to hypocentral distance for the available strong motion records of subduction zone interface earthquakes of NEI which are shown in Fig. 11a, b, respectively. Similarly, residuals for PGA and spectral acceleration (S_a) at 2.0 s are calculated using a finite-fault simulation model, as shown in Fig. 11c, d. It is seen from Figs. 10a, b and 11a–d that residuals

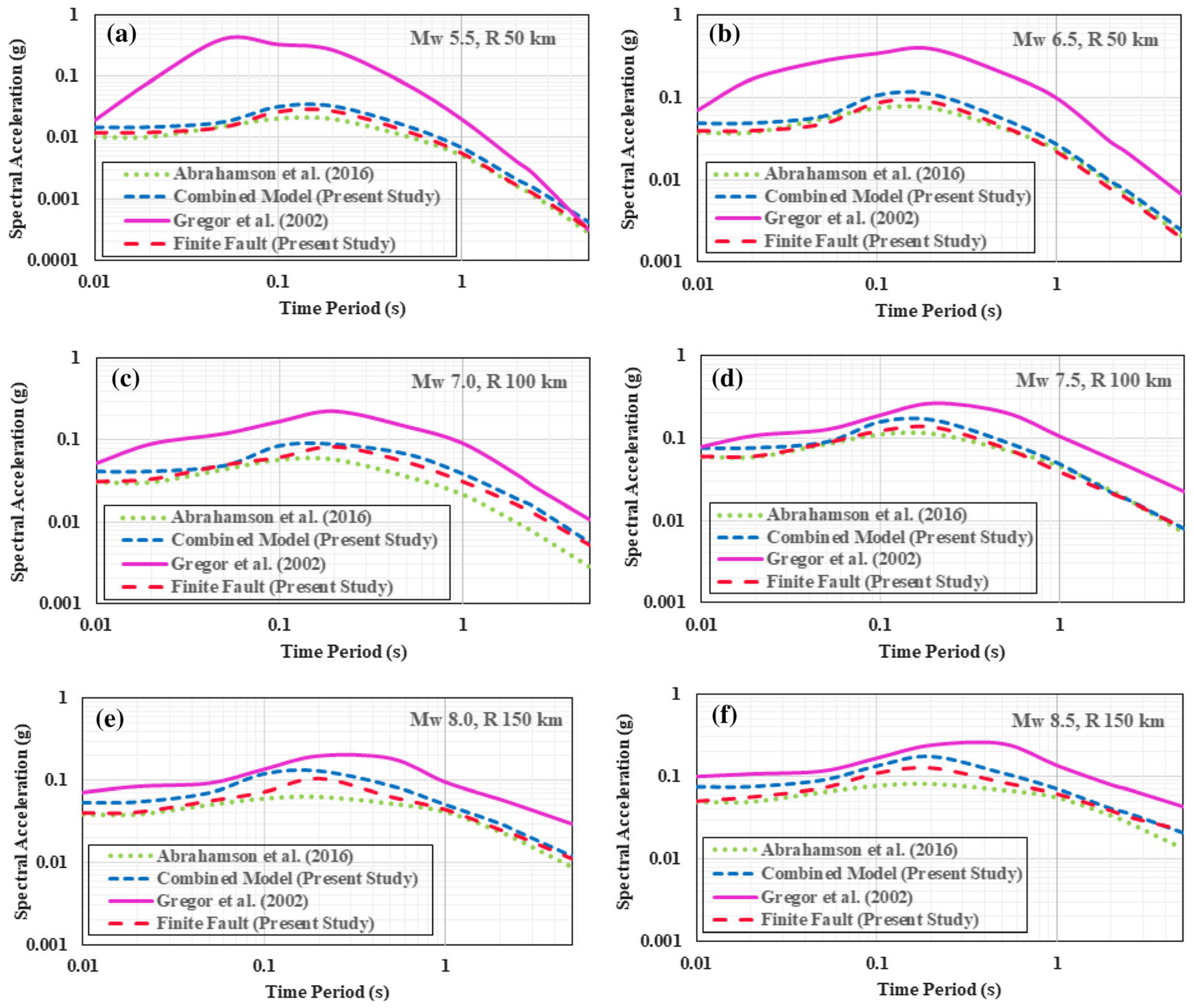

Figure 14
Comparison of spectral acceleration of the present GMM with Gregor et al.'s (2002) and Abrahamson et al.'s (2016) for M_w **a** 7.0, **b** 7.5, **c** 8.0 and **d** 8.5 at a hypocentral distances of 100 and 150 km w.r.t. time periods (0.01–5.0 s), respectively

of PGA and S_a with respect to magnitude and hypocentral distance are not biased.

The combined data set of the point-source model for M_w (4.5–6.5) and finite-fault modeling for M_w (6.5–9.0) was named the "Combined Model," as shown in Figs. 12, 13 and 14. We also compared our Combined Model with the finite-fault modeling in Figs. 12, 13 and 14.

We compared our model for the interface subduction zone earthquakes with the GMM of Gregor et al. (2002) and Abrahamson et al. (2016) for PGA with respect to hypocentral distance for magnitude M_w 5.5, 6.5, 7.0, 7.5, 8.0 and 8.5, as shown in Fig. 12a–f. We also compared S_a at 0.2 s for M_w 5.5, 6.5, 7.0, 7.5, 8.0 and 8.5 with respect to hypocentral distance, as shown in Fig. 13a–f. It is seen from Figs. 12 and 13 that Gregor et al.'s (2002) GMM gives higher S_a value than the present GMM. Our GMM gives higher value than Abrahamson et al.'s (2016) model.

We also compared our GMM for S_a at different time periods with the GMM of Gregor et al. (2002) and Abrahamson et al. (2016) for M_w 5.5, 6.5, 7.0, 7.5, 8.0 and 8.5 at hypocentral distances of 50, 50, 100, 100, 150 and 150 km, as shown in Fig. 14a–f, respectively. It is observed that our GMM gives lower values than the Gregor et al. (2002) and higher values than Abrahamson et al. (2016).

We compared our model both for point-source and finite-fault simulation models in Figs. 12, 13 and 14. It is observed from Figs. 12, 13 and 14 that ground motion parameters in a point-source seismological model give higher values as compared to a finite-fault simulation model. Point-source and finite-fault models differ in geometry of the source, definition and application of duration and normalization of finite sub-source summations (Atkinson et al. 2009). Boore (2009) stated that ground motion parameters simulated in a point-source model for a small and large earthquakes at close and far distances are substantially higher than the finite-fault simulation model for all frequencies.

It is observed from Figs. 12, 13 and 14 that our GMM based on both point-source and finite-fault models gives less PGA and S_a values as compared to Gregor et al.'s (2002) GMM. These differences may arise due to high value of V_{S30} used for our GMM. It is also observed from Figs. 12, 13 and 14 that PGA and S_a values in our model provide higher value in comparison to Abrahamson et al.'s (2016) GMM. This is due to the fact that in our model, we ignored forearc and backarc effects as these values are unknown for NEI and its adjacent countries. The averaged V_{S30} value for site class C in our GMM is also lower than that in Abrahamson et al.'s (2016) GMM. We expect the differences of ground motion parameter in the three GMMs are due to variations of region-specific seismic input parameters used to develop the model, such as quality factor, stress parameters and kappa factors.

9. *Conclusions*

In this study, we developed a new GMM for interface subduction zone earthquakes for NEI and its adjacent countries based on both point-source and finite-fault simulation models. Our GMM is based on 50,000 simulated ground motions for magnitude M_w 5.0–9.0 and hypocentral distances of 30–300 km. These ground motion samples are stochastically simulated based on region-specific seismic input parameters for NEI and its adjacent countries using Boore's point source model. Ground motions are also simulated based on a finite-fault simulation model using FINSIM.

Our model is best fitted with respect to both magnitude and hypocentral distance, and it will provide realistic ground motion parameters in NEI. Our GMM will also be useful in estimating seismic hazard of NEI and its adjacent countries.

10. *Data and Resources*

The strong ground motion databases used in this study are obtained from Das et al. (2006), Gupta (2010), Nath et al. (2012), Rahman (2012), Sil et al. (2015), the NEIC earthquake catalog and from other published sources listed in the references.

Acknowledgements

We would like to convey our gratitude to the Chief Editor, Fabio Romanelli, for giving us the opportunity to improve our manuscript based on the precious technical suggestions. We are also thankful to the potential reviewers for their valuable technical suggestions to improve our manuscript.

REFERENCES

Abrahamson, N. A., Gregor, N., & Addo, K. (2016). BC Hydro ground motion prediction equations for subduction earthquakes. *Earthquake Spectra, 32,* 23–44.

Anderson, J. G., & Hough, S. E. (1984). A model for the shape of Fourier Amplitude spectrum of acceleration at high frequencies. *Bulletin of Seismological Society of America, 74,* 1969–1993.

Atkinson, G. M. (2004). Empirical attenuation of ground motion spectral amplitudes in southeastern Canada and the northeastern United States. *Bulletin of Seismological Society of America, 94,* 1079–1095.

Atkinson, G. M., Assatourians, K., Boore, D. M., Campbell, K., & Motazedian, D. (2009). A guide to differences between stochastic point-source and stochastic finite-fault simulations. *Bulletin of Seismological Society of America, 99,* 3192–9201.

Atkinson, G. M., & Boore, D. M. (2003). Empirical ground-motion relations for subduction zone earthquakes and their application to Cascadia and other regions. *Bulletin of Seismological Society of America, 93,* 1703–1729.

Atkinson, G. M., & Silva, W. (2000). Stochastic modelling of California ground motions. *Bulletin of Seismological Society of America, 90*(2), 255–274.

Aung, H. H. (2015). *Myanmar earthquake history*. Myanmar: Wathan Press Yangon.

Ben-Menahem, A., Aboudi, E., & Schild, R. (1974). The source of the great Assam earthquake-an intraplate wedge motion. *Physics of the Earth and Planet Interiors, 9,* 265–289.

Beresnev, I. A., & Atkinson, G. M. (1998a). FINSIM-A FORTRAN program for simulating stochastic acceleration time histories from finite faults. *Seismological Research Letters, 69,* 27–32.

Beresnev, I. A., & Atkinson, G. M. (1998b). Stochastic finite fault model of ground motions from the 1994 Northridge, California, earthquake: I, validation non rock sites. *Bulletin of Seismological Society of America, 88,* 1392–1401.

Beresnev, I. A., & Atkinson, G. M. (1999). Generic finite-fault model for ground motions prediction in eastern North America. *Bulletin of Seismological Society of America, 89,* 608–625.

Boore, D. M. (1983). Stochastic of high frequency ground motions based on seismological models of the radiated spectra. *Bulletin of Seismological Society of America, 73,* 1856–1894.

Boore DM (1996) SMSIM Fortran program for simulating ground motions from earthquakes: Version 1.0. *U.S. Geological Survey Open File Report* 96:80-A.

Boore, D. M. (2003). Simulation of ground motion using the stochastic method. *Pure and Applied Geophysics, 160,* 635–676.

Boore, D. M. (2009). Comparing stochastic point-source and finite source ground motion simulations: SMSIM and EXSIM. *Bulletin of Seismological Society of America, 99,* 3202–3216.

Bora, D. K., Skolov, V. Y., & Wenzel, F. (2016). Validation of strong-motion stochastic model using observed ground motion records in North-east India. *Geomatics, Natural Hazards and Risks, 7,* 565–585.

Brune, J. N. (1970). Tectonic stress and the spectra of seismic shear waves from earthquakes. *Journal of Geophysical Research, 75,* 4997–5009.

Brune, J. N. (1971). Correction. *Journal of Geophysical Research, 76,* 5002.

Campbell, K. W. (2003). Prediction of strong ground motion using the hybrid empirical method and its use in the development of ground-motion (attenuation) relations in Eastern North America. *Bulletin of Seismological Society of America, 9,* 1012–1033.

Chen, W. P., & Molnar, P. (1983). Focal depths of intracontinental and intraplate earthquakes and their implications for the thermal and mechanical properties of the lithosphere. *Journal of Geophysical Research, 88,* 4183–4214.

Chhangte, R. L., Rahman, T., & Wong, I. G. (2020). Ground motion model for deep intraslab subduction zone earthquakes of Northeastern India and adjacent regions. *Bulletin of Seismological Society of America*. https://doi.org/10.1785/0120200050.

Das, S., Gupta, I. D., & Gupta, V. K. (2006). A probabilistic seismic hazard analysis of North-east India. *Earthquake Spectra, 22,* 1–27.

Drouet, S., Cotton, F., & Guéguen, P. (2010). V_{S30}, κ, regional attenuation and M_w from small magnitude events accelerograms. *Geophysical Journal International, 182,* 880–898.

Drouet, S., & Cotton, F. (2015). Regional stochastic GMPEs in low seismicity areas: Scaling and aleatory variability analysis—application to the French Alps. *Bulletin of Seismological Society of America, 105,* 1–20.

Goswami, H. C., & Sharma, S. K. (1982). Probabilistic earthquake expectancy in the northeast Indian region. *Bulletin of Seismological Society of America, 72,* 999–1009.

Gregor, N. J., Silva, W. J., Wong, I. G., & Youngs, R. R. (2002). Ground-motion attenuation relationships for Cascadia subduction zone megathrust earthquakes based on a stochastic finite-fault model. *Bulletin of Seismological Society of America, 92,* 1923–1932.

Gupta, I. D. (2010). Response spectral attenuation relations for in-slab earthquakes in Indo-Burmese subduction zone. *Soil Dynamics and Earthquake Engineering, 30,* 368–377.

Hanks, T. C., & Kanamori, H. (1979). A moment magnitude scale. *Journal of Geophysical Research, 84,* 2348–2350.

Hurukawa, N., & Maung, M. P. (2011). Two seismic gaps on the Sagaing Fault, Myanmar, derived from relocation of historical earthquakes since 1918. *Geophysical Research Letters, 38,* 1310–1314.

Iyengar, R. N., & Raghukanth, S. T. G. (2004). Attenuation of strong ground motion in peninsular India. *Seismological Research Letters, 75,* 530–539.

Joyner, W. B., & Boore, D. M. (1981). Peak horizontal Acceleration and velocity from strong motion records including records from the 1979, Imperial Valley, California earthquakes. *Bulletin of Seismological Society of America, 71,* 2011–2038.

Kayal, J. S., Arefiev, S., Baruah, S., Tatevossian, R., Gogoi, N., Sanoujam, M., et al. (2010). The 2009 Bhutan and Assam felt earthquakes (Mw 6.3 and 5.1) at the Kopili fault in the northeast Himalaya region. *Geomatics, Natural Hazards and Risk, 3,* 273–281.

Kempton, J. J., & Stewart, J. P. (2006). Prediction equations for significant duration of earthquake ground motions considering site and near-source effects. *Earthquake Spectra, 22,* 985–1013.

Kumar, A. V., Sangode, S. J., Kumar, R., & Siddaiah, N. S. (2005). Magnetic polarity stratigraphy of Plio-Pleistocene Pinjor formation(type locality), Siwalik group, NW Himalaya, India. *Current Science, 88,* 1453–1461.

Kundu, B., & Gahalaut, V. K. (2012). Earthquake occurrence processes in the Indo-Burmese wedge and Sagaing fault region. *Tectonophysics, 524,* 135–146.

Le Dain, A. Y., Tapponier, P., & Molnar, P. (1984). Active faulting and tectonics of Burma and surrounding regions. *Journal of Geophysical Research, 89,* 453–472.

Lin, P. S., & Lee, C. T. (2008). Ground-motion attenuation relationships for subduction-zone earthquakes in North-eastern Taiwan. *Bulletin of Seismological Society of America, 98,* 220–240.

Llenos, A. L., & McGuire, J. J. (2007). Influence of fore-arc structure on the extent of great subduction zone earthquakes. *Journal of Geophysical Research*. https://doi.org/10.1029/2007JB004944.

Mandal, P., & Rastogi, B. K. (1998). A frequency-dependent relation of Coda Qc for Koyna-Warna region, India. *Pure and Applied Geophysics, 153,* 163–177.

Mitra, S., Priestley, K., Bhattacharyya, A. K., & Gaur, V. K. (2005). Crustal structure and earthquake focal depths beneath North-East India and southern Tibet. *Geophysical Journal International, 160,* 227–248.

Mitra, S., Priestly, K., Gaur, V. K., & Rai, S. S. (2006). Frequency dependent Lg attenuation in the Indian platform. *Bulletin of Seismological Society of America, 96,* 2449–2456.

Molnar, P., & England, P. (1990). Surface uplift, uplift of rocks and exhumation of rocks. *Geology, 18,* 1173–1177.

Motazedian, D. (2006). Region-specific key seismic parameters for earthquakes in northern Iran. *Bulletin of Seismological Society of America, 96,* 1383–1395.

Motazedian, D., & Atkinson, G. (2005). Stochastic finite-fault model based on dynamic corner frequency. *Bulletin of Seismological Society of America, 95,* 995–1010.

Nandy, D. R. (1986). Geology and tectonics of Arakan Yoma—a reappraisal. *Regional Congress on Geology, Mineral and Energy Resources of Southeast Asia Bulletin, 20,* 137–148.

Nath, S. K., Thingbaijam, K. K. S., & Maiti, S. K. (2012). Ground-motion predictions in Shillong region, northeast India. *Journal of Seismology, 16,* 475–488.

Ni, J., & York, J. E. (1978). Late Cenozoic tectonics of the Tibetan plateau. *Journal of Geophysical Research, 83,* 5377–5384.

Ni, J. F., Guzman-Speziale, M., Beis, M., Holt, W. E., Wallace, T. C., & Seager, W. R. (1989). Accretionary tectonics of Burma and the three-dimensional geometry of Burma subduction zone. *Geology, 17,* 68–71.

Parvez, I. A., & Ram, A. (1997). Probabilistic assessment of earthquake hazards in the north-east Indian Peninsula and Hindukush region. *Pure Applied Geophysics, 149,* 731–746.

Raghukanth, S. T. G., & Somala, S. N. (2009). Modeling of strong-motion data in North-eastern India: *Q*, stress drop, and site amplification. *Bulletin of Seismological Society of America, 99,* 705–725.

Rahman, T. (2012). Seismological model parameters for the north-eastern and its surrounding region of India. *Earthquake Science, 25,* 323–338.

Raoof, M., Hermann, R., & Malagnini, L. (1999). Attenuation and excitation of three components ground motion in Southern California. *Bulletin of Seismological Society of America, 89,* 888–902.

Satyabala, S. P. (2002). The historical earthquakes of India. *International Geophysics, 81,* 797–798.

Satyabala, S. P. (2003). Oblique convergence in the Indo-Burma (Myanmar) subduction region. *Pure and Applied Geophysics, 160,* 1611–1650.

Seebar, L., & Armbruster, J. G. (1981). Great detachment earthquakes along the Himalayan arc and long-term forecasting. *American Geophysics Union, 4,* 259–277.

Sil, A., Sitharam, T. G., & Haider, S. T. (2015). Probabilistic models for forecasting earthquakes in the Northeast Region of India. *Bulletin of Seismological Society of America*. https://doi.org/10.1785/0120140361.

Singh, N. M., Rahman, T., & Wong, I. G. (2016). A new ground motion prediction model for north-eastern India crustal earthquakes. *Bulletin of Seismological Society of America, 106,* 1282–1297.

Singh, S. K., Ordaz, M., Dattatrayam, R. S., & Gupta, H. K. (1999). A spectral analysis of the 21 May 1997, Jabalpur, India earthquake (M_w 5.8) and estimation of ground motion from future earthquakes in the Indian shield region. *Bulletin of Seismological Society of America, 89,* 1620–1630.

Singh, S. K., Garcia, D., Pacheco, J. F., Valenzuela, R., Bansal, B. K., & Dattatrayam, R. S. (2004). Q of the Indian shield. *Bulletin of Seismological Society of America, 94,* 1564–1570.

Sokolov, V. Y., Loh, C. H., & Wen, K. L. (2002). Comparision of the Taiwan Chi-earthquake strong motion data and ground motion assessment based on spectral model from smaller earthquakes in Taiwan. *Bulletin of Seismological Society of America, 92,* 1855–1877.

Steckler, M. S., Mondal, D. R., Akhter, S. H., Seeber, L., Feng, L., Gale, J., et al. (2016). Locked and loading megathrust linked to active subduction beneath the Indo-Burman ranges. *Nature Geoscience, 9,* 615.

Strasser, F. O., Arango, M. C., & Bommer, J. J. (2010). Scaling of the source dimensions of interface and intraslab subduction zone earthquakes with moment magnitude. *Seismological Research Letters, 6,* 941–950.

Tavakoli, B., & Pezeshk, S. (2005). Empirical stochastic ground motion prediction for eastern North America. *Bulletin of Seismological Society of America, 95,* 2283–2296.

Tichelaar, S. W., & Ruff, L. J. (1993). Depth of seismic coupling along subduction zones. *Journal of Geophysical Research, 98,* 2017–2038.

Tiwari RK (2002) Status of seismicity in the North-eastern India and earthquakes disaster mitigation. *ENVIS Bulletin* **10(1)**: Himalayan Ecology.

Yenier, E., & Atkinson, G. M. (2014). Equivalent point-source modeling of moderate-to-large magnitude earthquakes and associated ground-motion saturation effects. *Bulletin of Seismological Society of America, 104*(3), 1458–1478.

Youngs, R. R., Silva, W. J., & Humphrey, J. R. (1997). Strong ground motion attenuation relationships for subduction zone earthquakes. *Seismological Research Letters, 69,* 58–73.

(Received March 6, 2020, revised February 2, 2021, accepted February 7, 2021, Published online March 8, 2021)